Author/s:
Knoop, MW;Deshpande, R;Schrijer, FFJ;Van Oudheusden, BW

Title:
Response of a turbulent boundary layer to steady, square-wave-type transverse wall-forcing

Date:
2025-06

Citation:
Knoop, M. W., Deshpande, R., Schrijer, F. F. J. & Van Oudheusden, B. W. (2025). Response of a turbulent boundary layer to steady, square-wave-type transverse wall-forcing. Physical Review Fluids, 10 (6), https://doi.org/10.1103/PhysRevFluids.10.064607.

Persistent Link:
https://hdl.handle.net/11343/356776

Response of a turbulent boundary layer to steady, square-wave-type transverse wall-forcing

Max W. Knoop [1,*] Rahul Deshpande [2] Ferry F. J. Schrijer [1] and Bas W. van Oudheusden [1]
[1] *Faculty of Aerospace Engineering, Delft University of Technology, 2629HS Delft, The Netherlands*
[2] *Department of Mechanical Engineering, The University of Melbourne, Parkville VIC 3010, Australia*

(Received 30 October 2024; accepted 4 April 2025; published 4 June 2025)

This study investigates the spatial evolution of a zero pressure gradient turbulent boundary layer (TBL) imposed by a square-wave (SqW) of steady spanwise wall-forcing, which varies along the streamwise direction (x). The SqW wall-forcing is imposed experimentally via a series of streamwise periodic belts running in opposite spanwise directions, following the methodology of Knoop *et al*. [Exp. Fluids **65**, 65 (2024)], with the streamwise extent increased to beyond ∼11 times the boundary layer thickness (δ_o) in the present study. This unique setup is leveraged to investigate the influence of viscous-scaled wavelength of SqW wall-forcing on the turbulent drag reduction efficacy for $\lambda_x^+ = 471$ (suboptimal), 942 (near-optimal), and 1884 (postoptimal conditions), at fixed viscous-scaled wall-forcing amplitude, $A^+ = 12$, and friction Reynolds number, $\mathrm{Re}_\tau = 960$. The TBL's response to this wall-forcing is elucidated by drawing inspiration from established knowledge on traditionally studied sinusoidal forcing, based on analysis of the streamwise-phase variation of the Stokes strain rate (SSR). The analysis reveals the SqW forcing to be characterized by a combination of two markedly different SSR regimes whose influence on the overlying turbulence is found to depend on the forcing waveform: subphase I of local and strong impulses of SSR downstream of the half- ($\lambda_x/2$) and full-phase (λ_x) locations, associated with a reversal in spanwise forcing directions, leading to significant turbulence attenuation, and subphase II of near-zero SSR over the remainder of forcing phase that enables turbulence recovery (when wall-forcing magnitudes and direction remain constant). Upon the initial imposition of the SqW forcing, the Reynolds stresses are strongly attenuated over the short streamwise extent of $x/\delta_0 < 0.5$ for all wavelengths, whereas the skin-friction transient is more gradual. Thereafter, once the forcing is ultimately established, the suboptimum and optimum wavelength regimes display no distinctive responses to the individual SSR subphases; rather, the drag-reduced TBL response is quasi-streamwise homogeneous. In contrast, an SSR-related phenomenology establishes itself clearly for the postoptimal case, in which a local attenuation of near-wall turbulence characterizes subphase I, while the turbulent energy recovers in subphase II owing to the extended region of near-zero SSR.

DOI: 10.1103/PhysRevFluids.10.064607

*Contact author: m.w.knoop@tudelft.nl

I. INTRODUCTION AND MOTIVATION

The ability to improve engineering efficiency, through manipulation of the turbulent skin-friction drag, has led to the proposal of several active and passive drag-reduction (DR) strategies in the literature. One of the most promising active flow control strategies, in terms of DR magnitudes, involves the imposition of a streamwise wave of spatiotemporal spanwise wall oscillations [1]. This strategy has been researched extensively over the past three decades across various possible implementations, as documented graphically in Fig. 1(a). This is primarily owing to its ability to yield significant DR with theoretical net power savings [1,2]. Notwithstanding, the practical deployment of this strategy on engineering systems, such as on aircraft wings or within oil pipelines, faces numerous challenges owing to its complex system architecture. One avenue that holds potential is the passive recreation of the spanwise forcing, e.g., through geometrical surface deformations such as oblique wavy walls [3] or dimpled surfaces [4]. Future design and/or optimization of such passive systems, however, can be significantly aided by understanding the fundamental flow physics over active wall-forcing scenarios, which forms the primary focus of this study.

The concept of streamwise traveling waves (STWs), introduced by Quadrio *et al.* [5], works by prescribing an oscillatory spanwise wall velocity following $W_w(x,t) = A\sin(k_x x - \omega t)$. Here A is the forcing amplitude of spanwise wall velocity, k_x and ω are the streamwise wave number and frequency, respectively, while t denotes time. We consider a Cartesian coordinate system where x, y, and z denote the streamwise, wall-normal, and spanwise directions, with corresponding instantaneous velocity components represented by U, V, and W, respectively. The STW forcing has a rich DR response in the k_x-ω space depicted in Fig. 1(b), commonly referred to as the "Quadrio map." The regime of downstream traveling waves ($\omega > 0$) comprises a ridge of significant DR (in green), as high as 38.4% for $A^+ = 12$ at $\mathrm{Re}_\tau = 906$ [6]. This is, however, flanked by a region of significant drag increase (in red), when the wave speed $c = \omega/k_x$ increases to the order of the convection velocity of the near-wall turbulence (i.e., $\mathcal{U}_c^+ \approx 10$ [7]). The superscript "+" here indicates viscous scaling based on the kinematic viscosity ν and the skin-friction velocity $U_\tau \equiv \sqrt{\tau_w/\rho}$, with τ_w being the wall-shear stress and ρ the fluid density. The friction Reynolds number is defined as $\mathrm{Re}_\tau \equiv \delta U_\tau/\nu$, corresponding to the ratio of the boundary layer thickness (δ) over the viscous length scale (ν/U_τ).

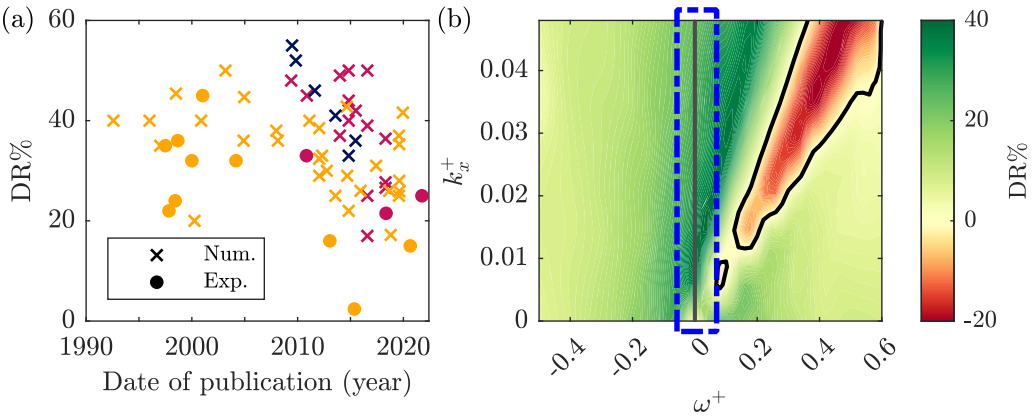

FIG. 1. (a) Maximum DR noted by various investigations of spanwise wall-forcings published in the last three decades. The forcing types are categorized according to streamwise traveling wave ($k_x \neq 0$, $\omega \neq 0$, magenta), time-oscillating ($k_x = 0$, orange), and spatial forcing ($\omega = 0$, dark blue). The data were obtained from the review of Ricco *et al.* [1]. (b) DR noted for a turbulent channel flow showcased in the form of the "Quadrio map," for the aforementioned three different forcing types in the k_x-ω space ($\omega = 0$ is highlighted by a dashed blue box). The map is recreated from the statistics shared by Gatti and Quadrio [6] for $A^+ = 12$ and $\mathrm{Re}_\tau = 906$, which closely matches the present experimental conditions. Terminologies are defined in Sec. I.

The STW reduces to a pure time-oscillating wall-forcing when $k_x = 0$, limiting the parameter space to the x axis in Fig. 1(b). This forcing was first investigated using direct numerical simulations (DNS) by Jung *et al.* [8], almost 17 years prior to the introduction of the STW. They found a DR of 40% on imposing forcing at $T^+ = 100$ ($T^+ = 2\pi/\omega^+$) and $A^+ = 12$ at $\mathrm{Re}_\tau = 200$, which was later corroborated experimentally by Laadhari *et al.* [9]. In general, it is evident from Fig. 1(a) that both STW ($k_x \neq 0$, $\omega \neq 0$) and time oscillating ($k_x = 0$) forcings have been investigated extensively in the literature, via both experimental and numerical approaches. Interestingly, however, very little attention has been paid to the pure spatial forcing ($\omega = 0$) scenario to date, having been considered by only six numerical studies (to the authors' knowledge), all of them limited to relatively low $\mathrm{Re}_\tau \leqslant 1600$ [10–15]. This forcing type corresponds to the vertical axis in Fig. 1(b), outlined by the blue dashed box, and forms the primary focus of this study. Spatial forcings have been typically imposed in the past by prescribing a steady spanwise wall velocity, W_w, that varies harmonically with the streamwise distance:

$$W_w(x) = A \sin(k_x x) = A \sin\left(\frac{2\pi}{\lambda_x} x\right), \tag{1}$$

with λ_x representing the streamwise actuation wavelength. Previous works of Viotti *et al.* [10] and Yakeno *et al.* [11] have highlighted several similarities between the spatial and time-oscillating forcings. For instance, the optimum DR for the former is found at $\lambda_x^+ \approx 1000$, which corresponds to $T^+ \approx 100$ under a convective transformation ($\lambda_x^+ = T^+ \mathcal{U}_c^+$) based on the nominal near-wall convection velocity mentioned previously ($\mathcal{U}_c^+ \approx 10$; [7]). However, the spatial forcing has been found to have a slightly higher DR potential than the time-oscillating forcing, with Viotti *et al.* [10] reporting DR ∼45% for $A^+ = 12$ at $\mathrm{Re}_\tau = 200$. This can be understood based on Fig. 1(b), where the time-oscillating forcing ($k_x = 0$) solely experiences a "footprint" of the high DR ridge. In contrast, the regime associated with spatial forcing ($\omega = 0$) "cuts" through the high DR ridge, offering a conservative alternative to the STW forcing by avoiding the drag-increasing regime altogether.

A further benefit of a purely spatial forcing, compared to the STW forcing, also becomes apparent when considering the practical realizability of the associated wall-forcing setups. Past experimental studies [16–18] investigating STW forcing considered discrete wall elements oscillating periodically along the spanwise/azimuthal direction at a particular x location. This requires a much more complex system architecture than for a spatial forcing setup where the local spanwise wall velocity is constant (i.e., nonoscillatory). This makes the latter more practically feasible when it comes to recreation through active (or passive) devices. In the case of flat-plate turbulent boundary layers (TBL), for instance, spatial forcing can be imposed "actively" by using a series of steady spanwise running wall segments, similar to that realized in the study of Kiesow and Plesniak [19]. This concept is graphically depicted in Fig. 2 where the idealized sinusoidal wave [SinW; Eq. (1)] forcing is shown, alongside its simplified and discretized version through a square-wave (SqW) forcing. The choice of the latter was motivated from the standpoint of practical realizability of such an experimental setup, as also adopted by past STW experimental studies [16–18]. Obviously, the SqW forcing does not affect the overlying turbulent flow in the exact same way as a SinW forcing, since it comes with a number of implications, which have been pointed out by past investigations [16,20], namely, (i) the cumulative forcing intensity, defined by the average of the wall-velocity (W_w) magnitude, being higher for a SqW than a SinW for the same amplitude and (ii) an impulsive change in phase from positive to negative spanwise wall velocities in the case of a SqW.

A preliminary version of a wall-forcing setup, similar to Fig. 2, using four subsequent spanwise running belts, has been realized and validated previously by the present authors [21]. The concept of this setup offers the unique capability to change the forcing wavelength (λ_x) independent of the forcing amplitude (A). This is made possible by the ability to vary λ_x simply by changing the number of wall elements (i.e., belts) S, which make up one complete periodic waveform, while A is manipulated by controlling the speed of the belts. Figure 2 schematically depicts the wavelength variation from (a) $S = 2$ to (b) $S = 8$, thereby permitting the forcing λ_x for the latter to be four times that of the

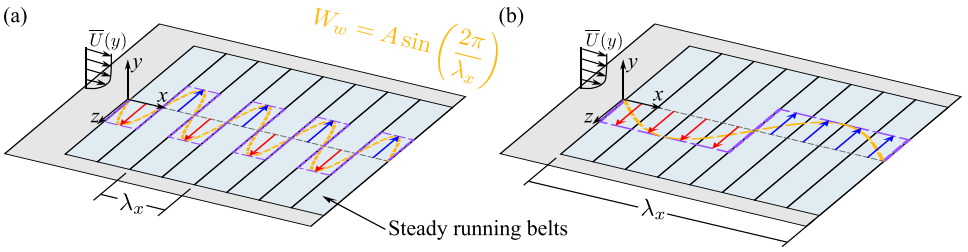

FIG. 2. Schematic of the spatial wall-forcing imposed in the form of a steady sinusoidal wave (SinW; orange) in past simulation studies, compared against steady square-wave (SqW; purple) forcings achieved in experiments through discretized wall elements (light blue). Spatial forcing in (b) corresponds to a wavelength λ_x that is four times that in (a). Red and blue arrows, respectively, indicate positive and negative spanwise wall velocities (W_w).

former. This setup thus enables independent investigation of the influence of viscous-scaled forcing magnitudes (A^+) and forcing parameter (wavelength; λ_x^+) on the overlying TBL, which is otherwise challenging to achieve in the case of time-oscillating forcing setups where these parameters, A^+ and ω^+ (or T^+), are commonly coupled. Such investigations could be of particular interest in light of the recent work by Marusic and co-workers [2,18,22], which reported significant DR with theoretical net power savings for a high Reynolds number TBL [of order $\mathrm{Re}_\tau = O(1 \times 10^4)$], based on STW forcings. Their work adopted two different approaches of imposing STW forcings: the first involved imposing wall frequencies tuned to the small-timescale/large-frequency motions via the inner-scaled actuation (ISA) strategy [i.e., $\lambda_x^+ = O(1000)$], while the second affected the large-timescale/small-frequency ($\lambda_x^+ \gg 1000$) motions via the outer-scaled actuation strategy.

Forcing applied to a spatially developing TBL also presents the opportunity to study the initial transients at the onset of actuation, which allows us to further our understanding of the DR mechanism. For instance, in the case of temporal wall-forcing, Ricco and Wu [23] have shown experimentally that the DR exhibits a streamwise transient of $4 - 5\ \delta$, before reaching a more or less "fully developed" state in the TBL. In general, the available literature [1] suggests the relevant scaling parameter for the streamwise transient length to be δ, rather than a forcing-related parameter (e.g., T^+, λ_x^+) or an inner scaling. Such an initial spatial transient analysis, however, is not possible through conventional fully developed channel flow simulations, which have been predominantly considered for investigating spatial wall-forcings in the past. Further, while the majority of the past research has primarily focused on sinusoidal wave (SinW) forcing, the present study aims to explore, in particular, the streamwise transient response of a TBL to square-wave (SqW) wall-forcing, as motivated above by viewpoints from both fundamental (drag reducing mechanism) and practical (realizability) perspectives.

To this end, particle image velocimetry is conducted across a large streamwise fetch of the zero-pressure gradient (ZPG) TBL, which is exposed to a steady spanwise wall-forcing along a SqW pattern in x. Through these unique experiments, the paper aims to further our understanding of the DR mechanisms specific to SqW forcing, by documenting its phasewise (spatial) turbulence modification, and contrasting it to that reported previously in the literature for SinW forcings [24,25]. Throughout this paper, we will be using "phasewise" variation to correspond to the flow variation over the streamwise periodic domain: $0 \leqslant x \leqslant \lambda_x$. The present experiments will differentiate the spatial evolution of turbulence modification imposed via spatial wall-forcing in relation to wavelength variation, where we consider three regimes of suboptimal, optimal, and postoptimal forcing. As remarked previously, such an investigation is made possible via the independent variation of the actuation wavelength. These insights would potentially be instrumental in developing passive forcing techniques in the future.

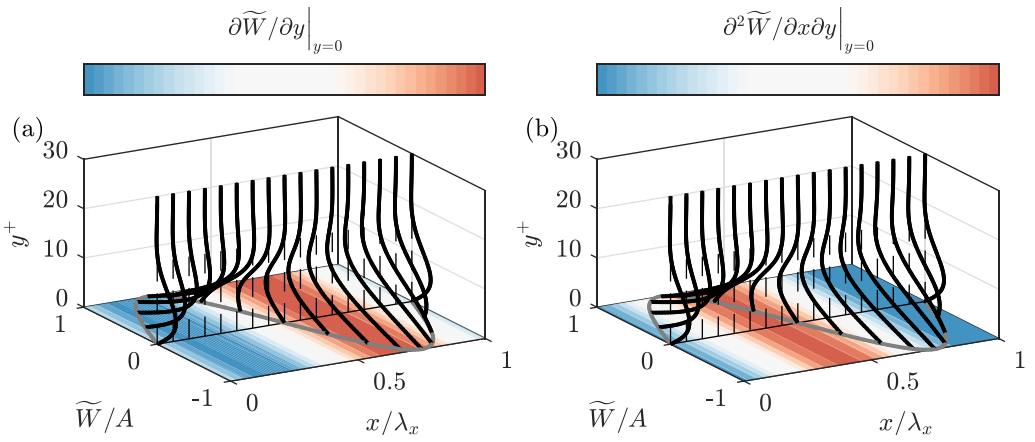

FIG. 3. An example of the spanwise velocity profiles of the spatial Stokes layer for sinusoidal spanwise forcing. The gray lines denote the spanwise wall velocity ($\widetilde{W}_w$), and the black lines are representative of the wall-normal $\widetilde{W}$ profiles. The wall-based phasewise variation of (a) the Stokes strain ($\partial\widetilde{W}/\partial y|_{y=0}$) and (b) the SSR ($\partial^2\widetilde{W}/\partial y\partial x|_{y=0}$) have been visualized by the colored contours. The red and blue regions denote high SSR magnitude in (b), which corresponds with the negligible values of Stokes strain in (a). Vice versa, near-zero SSR is associated with a region of lingering (i.e., maximum) Stokes strain in (a).

With regard to the organization of this paper, we first introduce the literature discussing the state-of-the-art understanding of achieving turbulence control and DR through SinW forcings in Sec. I A. The details and methodology of our experimental setup are then presented in Sec. II. The experimental results are documented in Sec. III. We begin by analyzing the observed initial transient of the spatial modification of turbulence at the start of SqW forcing in Sec. III A. Subsequently, in Sec. III B we provide a model to assess the rate of change of Stokes strain that was previously correlated with the phasewise turbulence modification for a SinW. Hereafter, in Sec. III C we detail the implications of the established SqW-specific forcing on the modification of turbulence and skin friction at the initiation of forcing. Our observations in relation to these forcing mechanisms are later substantiated in Sec. III D, in the domain where the wall-forcing is fully established. We conclude the results section by discussing the overall flow control efficacy of the SqW forcing via estimation of the nominal DR as a function of λ_x^+, in Sec. III E. A conceptual overview of the flow phenomenology associated with SqW forcing is elaborated upon in Sec. IV, followed by a discussion of its implications for the two waveform types and an outlook on the remaining related research questions of interest.

A. The mechanism of drag reduction for sinusoidal transverse forcing

Numerous efforts have been made over the past decade to describe the flow physics underlying STW forcings [1,24–27], but the exact mechanism behind their DR efficacy still remains largely unidentified. Here we briefly review some literature that has hypothesized plausible DR mechanisms for spanwise forcings imposed via a SinW configuration. This will be used as a reference in Sec. III B to compare and contrast with findings based on the SqW forcing configuration considered in the present study. In the remainder of this paper, statistical quantities may be subjected to a triple decomposition of the instantaneous velocity components, corresponding to $U = \overline{U} + \widetilde{U} + u$ (and correspondingly for V and W). The $\overline{\cdots}$ operator corresponds to the long-time averaged mean, whereas $\widetilde{\cdots}$ denotes the phase-averaged quantities associated with the periodic forcing (temporal or spatial), and u corresponds to the stochastic fluctuations. Similarly, the vorticity component associated with coordinate i is decomposed as $\Omega_i = \overline{\Omega_i} + \widetilde{\Omega_i} + \omega_i$.

Following the first numerical simulations of the time-oscillating forcing by Jung *et al.* [8], Akhavan *et al.* [28] and Baron and Quadrio [29] proposed that the wall-normal gradient of the spanwise velocity ($\partial\widetilde{W}/\partial y$; i.e., the Stokes strain) is responsible for spatially decorrelating the low-speed streaks from the overlying quasi-streamwise vortices (QSVs). This decorrelation is a consequence of the reorientation of the near-wall velocity streaks into the direction of the mean strain (i.e., the vector $[\partial\widetilde{U}/\partial y\ 0\ \partial\widetilde{W}/\partial y]$), as was also noted by Touber and Leschziner [24]. It leads to the dampening of the self-sustaining cycle responsible for the majority of the near-wall turbulence kinetic energy production [7,30], which was also noted experimentally by Ricco [31] and Kempaiah *et al.* [32]. For reference, a phasewise distribution of Stokes strain has been depicted by the colored contours in Fig. 3(a), and compared against the corresponding spatial forcing; the wall-velocity $\widetilde{W}_w$ and its $\widetilde{W}$ profiles are shown in gray and black, respectively. Imposition of the Stokes strain also results in a phase-averaged streamwise vorticity component ($\widetilde{\Omega}_x = \partial\widetilde{W}/\partial y$). Choi and Clayton [33] hypothesized that $\widetilde{\Omega}_x$ gets periodically tilted by the imposed Stokes motion, giving rise to a (negative) net spanwise vorticity component ($\widetilde{\Omega}_z$) centered around $y^+ \simeq 15$. By induction, this reduces the momentum at the wall (causing a drop in wall-shear stress) while increasing it in the upper part of the buffer layer (causing an overshoot of the mean streamwise velocity profile). Several studies [11,34,35] have investigated the subsequent modification to the QSVs, which is central to the shear-stress producing mechanism [36]. They found the QSVs to shift in the positive wall-normal direction while reducing their energetic content, thereby dampening the near-wall dynamics.

Interestingly, recent studies from Leschziner and co-workers [24–26] have reported dampening of the near-wall streaks to be dependent on the rate of change in the Stokes strain. The spatial forcing considered here can be quantified by the Stokes strain rate (SSR; $\partial^2\widetilde{W}/\partial y\partial x$), of which a phasewise distribution at the wall has been depicted by the colored contours in Fig. 3(b). For instance, Agostini *et al.* [25] highlighted the significance of the SSR in the manipulation of the near-wall vorticity dynamics for postoptimal forcing at $T^+ = 200$. They hypothesized that the wall-normal vorticity is redistributed into spanwise vorticity in regions of strong SSR, through vortex stretching and tilting phenomena. This redistribution of vorticity dampens the near-wall streaks, subsequently attenuating the QSVs and the wall-shear stress in accordance with the dynamics of the self-sustaining cycle [30]. From a physical point of view, the regions of high SSR correspond to the phases where the spanwise shear strain reverses in sign. Previous studies have found the near-wall streaks to dampen much more intensely during phases of high SSR magnitude, while the streaks tend to recover in the absence of Stokes strain variation (i.e., SSR ≈ 0). These interpretations are consistent with earlier investigations of constant straining conditions by Bradshaw and Pontikos [37], who associated the recovery in the near-wall turbulence to the reestablishment of an internal boundary layer, along the direction of the near-constant (i.e., "lingering") Stokes strain. It is worth emphasizing here that the phasewise variation of C_f for postoptimal actuation does not "directly" respond to the imposed SSR; rather, Agostini *et al.* [25] report C_f to increase in the region of high SSR at the wall, while it declines in the following lingering domain. More recently, Deshpande *et al.* [22] also investigated the lingering of the Stokes strain, in the case of STW forcings imposed on a high Re_τ TBL, by quantifying the instantaneous flow angle in the wall-parallel plane. They found an increase in T^+ (which was coupled with reduced A^+) to result in the prolonged lingering of the flow angle, which correlated with the decrease in DR. Analogous to the concept of SSR, Ding *et al.* [38] recently introduced an "acceleration" parameter ($a^+ = A^+/T^+$) for temporal SinW forcing, which was shown to scale the DR very well. The key takeaway from most recent studies on spatiotemporal wall-forcing, hence, is that the SSR and its phasewise variation influence the turbulence modification and skin friction distinctly. Later in Secs. III B and III C, we use this well-established understanding of the phasewise variation of the SSR (for SinW forcing) to compare against our observations for the SqW forcing, to explain the overlying turbulent flow modification.

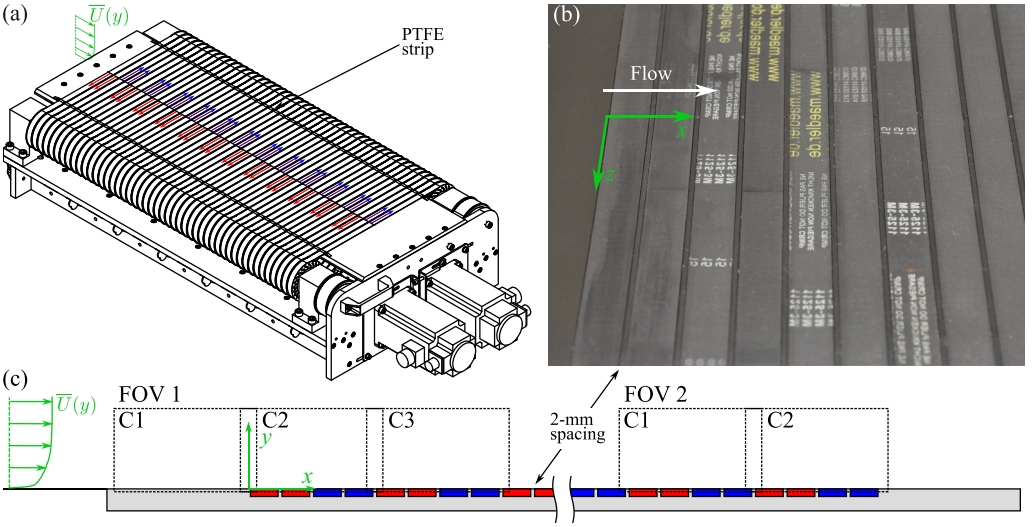

FIG. 4. (a) Schematic of the experimental apparatus developed to impose spatial SqW wall-forcing. (b) Photograph of the actuation surface and belts at the inflow. (c) Schematic representation of the PIV setup in the streamwise-wall-normal plane. The dotted boxes indicate the field of view (FOV) of individual cameras (C1–3), which are used to capture the flow in the upstream and downstream sections of the spatial wall-forcing setup. Colored arrows and belts in (a) and (c) indicate positive (red) and negatively (blue) oriented W_w vectors for a SqW waveform of $S = 4$.

II. EXPERIMENTAL DETAILS

The experiments were performed in a subsonic open return wind tunnel at the Delft University of Technology, featuring a 4:1 contraction ratio. A flat plate turbulent boundary layer test section is employed downstream of the tunnel contraction, having a cross section of 0.6×0.6 m^2 and a development length of $\sim$2.5 m upstream of the actuation surface. The boundary layer is tripped to a turbulent state at the leading edge of the flat plate by a 0.12 m roughness strip of 40-grit sandpaper. A zero pressure gradient was ensured along the entire streamwise direction by adjusting the flexible top wall to the acceleration parameter [39], $K \equiv (\nu/U_e)^2(\mathrm{d}U_e/\mathrm{d}x)$, such that a value of $K < 1.6 \times 10^{-7}$ is maintained under all operating conditions [40], where U_e is the velocity at the edge of the boundary layer. A further detailed description of the boundary layer test section and its accompanying characteristics can be found in Dacome *et al.* [40].

A. Spatial wall-forcing apparatus

This study deploys the concept of steady running belts in opposing spanwise direction [19], discussed in Sec. I, for the experimental realization of the square-wave forcing setup. While a preliminary version of this setup has been reported previously in Knoop *et al.* [21], here we present an extended version of the same concept that can affect the boundary layer for a much longer streamwise fetch. The spatial forcing setup [Fig. 4(a)] comprises 48 belts extending across $\sim$800 mm ($>11\delta_0$, with δ_0 representing the TBL thickness for the nonactuated flow scenario; Table I) in the streamwise direction, making it $\sim$20 times longer than our previous setup. This permits detailed investigations of the initial streamwise transients of the skin-friction drag and the overlying turbulent flow statistics along the wall-normal direction, followed by their steady-state/fully developed characteristics. The actuating surface comprises neoprene belts with a streamwise extent of 15 mm and spanning $\sim$ 294 mm ($>4\delta_0$) in width on the test section floor. Subsequent belts are equally spaced along the streamwise direction with a spacing of 2 mm, which was the smallest possible

TABLE I. Overview of the experimental conditions and actuation parameters.

Inflow boundary layer characteristics				Actuation characteristics					
U_∞ (m/s)	$U_{\tau 0}$ (m/s)	δ_0 (mm)	Re_τ	S	λ_x (mm)	A (m/s)	λ_x^+	A^+	Line style
5	0.207	69.9	960	–	–	–	–	–	
5	0.207	69.9	960	2	34	2.46	471	12.0	
5	0.207	69.9	960	4	68	2.46	942	12.0	
5	0.207	69.9	960	8	136	2.46	1884	12.0	

distance realizable during setup fabrication. Such a spacing was necessary to recess each belt into dedicated spanwise surface grooves, which ensured the actuation surface is flush with the wind tunnel flooring [schematically depicted in Fig. 4(c)]. Strict tolerances were maintained on the actuation surface, with a maximum of 50 μm for the gap and step sizes. Figure 4(b) shows a photograph of the actuation surface at the inflow station, presenting an actual view of the belts embedded in the surface plate. Interested readers can also refer to a video recording of the actuated surface, which has been made available as supplemental material [41].

The surface roughness of the neoprene belts is slightly higher compared to the upstream and downstream aluminum surface plate (i.e., tunnel floor). However, it is within the tolerance limit for being considered as hydrodynamically smooth, with $k^+ \leqslant 5$ for the flow Re_τ under consideration [42]. The belts were constrained within the spanwise grooves (i.e., flush with the wall) by two PTFE strips that were bolted on each spanwise edge of the setup [Fig. 4(a)]. Despite this, some vibration and vertical displacement of the belts were observed to occur, which were characterized by a PSV-500 Poltec scanning vibrometer. For the actuation conditions in the current study, the worst scenario was found to be a 39 μm standard deviation of the wall-normal displacement, while the median displacement across the full actuation surface was 13 μm, both of which are within one viscous unit which is approximately 72 μm. Regardless of the influence of the surface imperfection, a slight modulation of the near-wall turbulence was still observable in the final results (see, e.g., Figs. 7 and 11). These do not, however, affect our major findings/conclusions since we primarily contrast the flow physics for the actuated surface against those over the same surface in the nonactuated scenario.

Rotation to drive the belts is provided by two 6 Nm servo motors (LCMT-18L02), one for each spanwise direction, which can achieve a maximum spanwise velocity of 6 m/s. It is important to highlight the fact that the belts are driven in a steady fashion, following the prescription of a SqW spatial forcing sketched in Fig. 2 previously. The motors are connected to two driving axes, including a nonslip pulley system that drives the belts directly. The pulleys can be connected or disconnected to the axis by employing a fixation mechanism, allowing interchangeability of the spanwise direction of the individual belts ($\pm W_w$). This unique feature permits the investigation of varying actuation/forcing wavelengths on the overlying TBL, as sketched previously in Fig. 2. We will denote the number of belt elements that make up a periodic waveform (λ_x) as "S." Considering the length of one belt "element" (l_S) as a combination of the belt's streamwise extent and periodic spacing/gap (i.e., $l_S = 17$ mm), the actuation wavelength $\lambda_x = S \times l_S$. For convenience in the discussion of the results, we fix the origin of the coordinate system at 1 mm upstream of the first belt. On some occasions, we will discuss the integral effect of surface actuation by streamwise averaging of the considered flow property across the entire spatial phase (i.e., λ_x), which will be denoted by the $\langle ... \rangle_x$ operator.

B. Particle image velocimetry

Multi-camera planar PIV measurements (2D-2C) were conducted in the streamwise-wall-normal plane (x-y) to quantify the corresponding velocity components in a wide field of view (FOV).

An overlap of ∼15 mm between adjacent camera views was retained to allow for stitching of the individual vector fields. Such wide FOV measurements were conducted both close to the start (FOV1) as well as towards the end (FOV2) of the actuation surface, as depicted schematically in Fig. 4(c), independent of each other. FOV1 captures nominally ∼70 mm of the inflow over the tunnel wall followed by that over belts no. 1–8, using three sCMOS cameras (C1–C3) in a row, to image $\sim 210 \times 49$ mm^2 in the streamwise and wall-normal directions, respectively. This configuration enables investigation of the initial streamwise transients of the TBL flow for the wall-actuated cases. On the other hand, FOV2 captures the flow field over belts no. 40–48, employing two cameras (C1 and C2) so as to image $\sim 140 \times 49$ mm^2. As discussed later in Sec. III, the TBL drag and flow statistics are found to be nominally saturated at the belt locations in FOV2 and, as such, represent a fully developed regime of actuation. This methodology provides the flow field statistics that permit quantification of the DR, as well as the turbulent stresses, for the various spatial forcing scenarios investigated in this study. While previous studies have investigated the energy and vorticity budgets to understand drag-reducing mechanisms [25,26,34], our current experimental, with its relatively large field of view (FOV) and the absence of higher spatial and temporal fidelity, prevents such detailed analysis. Henceforth, our primary focus is to characterize the streamwise evolution of the turbulent stresses to wall-forcing.

For data acquisition, digital LaVision sCMOS cameras (2160×2560 px^2, 16 bit, 6.5 μm) were used to acquire 2000 uncorrelated particle image pairs at a sampling frequency of 8 Hz ($1/\Delta t$). The individual image pairs are, hence, separated by about nine boundary layer turnovers times ($\delta_0/U_\infty \Delta t$). Nikkor AF-S 200 mm lenses were used at an f/5.6 aperture. A time separation between image pairs of 50 μs was selected to achieve particle displacements of ∼9 pixels in the freestream. Resulting from the wall-motion, the maximum out-of-plane movement was ∼0.12 mm, corresponding to about one-eighth of the laser sheet thickness. We consider this to be sufficiently within acceptable limits. Illumination was provided by Quantel Evergreen 200 laser (Nd:Yag, 532 nm, 200 mJ) at 75% power setting. Laser optics were employed to create a laser sheet of ∼1 mm thickness. Seeding was generated using a SAFEX Fog 2010+ fog generator to inject 1 μm water-glycol tracer particles into the air stream.

The PIV images were processed using DaVis 10.2 software. It involved spatial filtering by subtracting a sliding Gaussian average, having a kernel width of 6 pixels, followed by a normalization with the local average over an 11-pixel kernel. Vector calculations were done using a cross-correlation algorithm, employing circular Gaussian interrogation windows of 16×16 pixels at 75% overlap. This resulted in the final spatial resolution of the PIV interrogation window to be of the order of 0.45 mm or 6.2 $\nu/U_{\tau 0}$, where $U_{\tau 0}$ is the friction velocity associated with the nonactuated flow. The universal outlier detection algorithm [43] was utilized for vector validation, with a 2-times median filter to remove vectors with a residual above 2. Given the overlap, a vector pitch of 0.11 mm or 1.6 $\nu/U_{\tau 0}$ was achieved.

A total of four cases are discussed in the current study (refer to Table I), namely, a nonactuated case and three cases corresponding to varying streamwise actuation wavelengths: $\lambda_x^+ = \lambda_x U_{\tau 0}/\nu = 471,\ 942$, and 1884. These wavelengths were achieved by changing the number of belt elements in the waveform to $S = 2$, 4, and 8. This wavelength range has been chosen strategically to cover the domain both greater and lower than the optimum of $\lambda_x^+ \approx 1000$ [10,11]. The same inflow condition of tunnel freestream, $U_\infty \approx 5$ m/s, and a belt speed of 2.46 m/s, were maintained across all cases, resulting in a constant spatial forcing magnitude $A^+ = A/U_{\tau 0} = 12$.

C. Scaling of the mean velocity profiles and turbulent drag reduction

Comparison between the mean velocity profiles for actuated and nonactuated cases can be made by the use of two different velocity scalings, either (i) the reference friction velocity $U_{\tau 0}$ of the nonactuated case or (ii) the actual friction velocity of the individual cases U_τ. Throughout this study, we will follow the convention to denote normalization by the respective velocity scales via the superscripts "+" and "*." It is now well known [6] that normalizing the mean velocity profile

by reference $U_{\tau 0}$ results in a collapse in the outer layer, while using the actual U_τ yields a collapse in the viscous sublayer, along with an upward shift in the logarithmic layer (in case of DR).

The large extent of the PIV FOV, combined with the measurement uncertainty in the near-wall region, results in a lack of reliable data in the viscous sublayer ($y^+ \leqslant 5$). Hence, accurate estimation of the skin friction directly from the gradient of the mean velocity profile ($\mathrm{d}\overline{U}/\mathrm{d}y|_{y=0}$) is not feasible. Instead, we can obtain U_τ indirectly for the actuated cases by fitting the mean velocity profiles to a modified composite profile, inspired from the original proposal of Chauhan *et al.* [44]. To this end, we modify the composite formulation to accommodate for the additional ΔB shift that is expected to occur when normalization is made with the actual U_τ [6]. Further details on the modified composite fitting procedures are outlined in Appendix A, where we discuss the efficacy of the method and implications of the modified fit.

Accordingly, the drag reduction (DR) can be expressed as the percentage difference of wall-shear stress with respect to the nonactuated case, which can also be expressed in terms of U_τ (assuming equal freestream velocity and density), according to

$$\mathrm{DR}\% = \frac{\tau_{w0} - \tau_w}{\tau_{w0}} \times 100 = \left[1 - \left(\frac{U_\tau}{U_{\tau 0}}\right)^2\right] \times 100. \tag{2}$$

Standard uncertainty propagation is applied to the U_τ components to obtain a 95% confidence interval on the DR and the skin-friction coefficient, $C_f \equiv 2(U_\tau/U_\infty)^2$. In its canonical formulation, a narrow 95% confidence interval U_τ of $\pm 0.7\%$ was found [45]. Similarly, we assessed the uncertainty of the modified fit from our actuated flow data in FOV2, which was found to be of similar order at $U_\tau \pm 0.75\%$ (refer to Appendix A for further details). It is important to recognize that our evaluation of DR is not a direct measurement; as such, we do not treat the DR and C_f as absolute values, but rather use them for purposes of qualitative assessment. The qualitative trends are reproduced reliably through the aforementioned procedure, which is evidenced by their consistency with the existing literature (see, e.g., Figs. 6, 8, 11).

D. Inflow boundary layer characteristics

We begin by analyzing the turbulent boundary layer characteristics at the inflow upstream of the actuation surface to validate our PIV measurements and assess the canonical structure of the boundary layer. For this, we conduct ensemble and streamwise averaging of the velocity statistics to improve the statistical convergence of the data in the region $-11\ \mathrm{mm} \leqslant x \leqslant -1\ \mathrm{mm}$, corresponding to FOV1 [Fig. 4(c); $x = 0$ is immediately upstream of the first belt]. The friction velocity ($U_{\tau 0}$) was found to be $U_{\tau 0} \approx 0.207$ m/s via the composite profile method of Chauhan *et al.* [44], of which details are provided in Appendix A. Since the present FOV1 does not extend across the entire TBL thickness in wall-normal direction, a separate PIV experiment was conducted (not discussed for brevity) to yield $\delta_0 = 69.9$ mm and $\mathrm{Re}_\tau = 960$. Figures 5(a) and 5(b) depict profiles of the mean streamwise velocity and the Reynolds stresses from the PIV data, respectively (in black circles). These are compared against the profiles from the direct numerical simulation (DNS; in gray lines) of a ZPG TBL at a comparable $\mathrm{Re}_\tau = 974$ [46]. This confirms that the inflow TBL is canonical in nature, displaying only minor deviations from the DNS profiles, which are likely caused by the limitations of the PIV measurement technique. For instance, the disagreement of the near-wall $\overline{U}^+$ profile, below $y^+ < 4$, is attributed to biased velocity measurements owing to the PIV interrogation window partly overlapping the wall. The Reynolds stresses also exhibit a similar discrepancy in this region. The streamwise normal stress shows the largest deviation from the DNS reference, with an attenuation of the near-wall peak. Moreover, a slight variation in the outer layer is observed, attributed to the higher Re_τ of the DNS reference. The disagreement in the near-wall region can be attributed to the attenuation of the small-scale energy due to finite-sized PIV interrogation windows and laser-sheet thickness, which is well known from the literature [47]. The characteristic near-wall peak in the $\overline{uu}^+$ profile is nevertheless found at the appropriate location

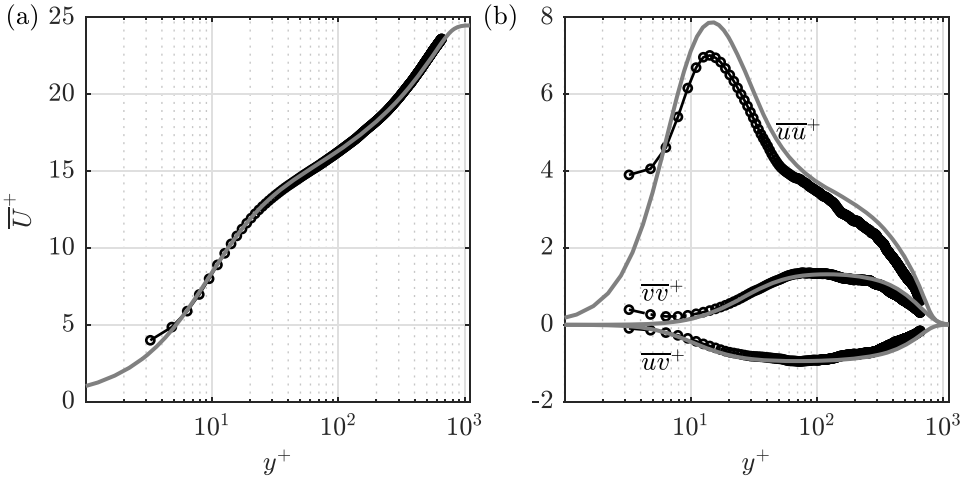

FIG. 5. Wall-normal profiles of (a) mean streamwise velocity, $\overline{U}^+$ and the (b) Reynolds stresses $\overline{uu}^+$, $\overline{vv}^+$, and $\overline{uv}^+$ averaged across -11 mm $\leqslant x \leqslant -1$ mm from the PIV FOV1, measured upstream of the actuation setup. The gray solid lines are from the ZPG TBL DNS at $\mathrm{Re}_\tau = 1060$ (with δ based on the composite fit) [46].

of $y^+ = 15$, demonstrating consistency with expected TBL statistics. The limited dynamic range of PIV measurements for the V component may introduce small-scale spurious fluctuations [48] resulting in a minor energy increase, plausibly explaining why the $\overline{uv}^+$ and $\overline{vv}^+$ components show no significant spatial attenuation despite expectations. However, we are primarily concerned with larger-scale flow phenomena that are unaffected by these small scales and always contrast against a nonactuated reference; as such, these do not affect our conclusions.

III. RESULTS

A. Streamwise evolution of turbulence statistics at the initiation of spatial forcing

We investigate the initial streamwise transients of the actuated ZPG TBL over the upstream portion of the setup at $\mathrm{Re}_\tau = 960$. For this, we consider PIV measurements from FOV1. This FOV covers a part of the inflow along with the first eight belts, which cover a streamwise extent of $\sim 2\delta_0$, measured from the leading edge of the actuation surface. We compare first the nonactuated case to the near-optimum wall-forcing case, i.e., $\lambda_x^+ = 942$, having the maximum DR $\sim$38% (as will be quantified and discussed later in Sec. III E). The downstream development of $\overline{U}^*$ is first evaluated, with the skin friction obtained via the modified composite fit procedure (Appendix A). Figures 6(a)–6(h) present $\overline{U}^*$ corresponding to the center of each of the eight belts in FOV1, which are obtained by spatially averaging $\overline{U}$ over a region of $\Delta x \sim \pm 0.007\delta_0 \sim \pm 6.9\nu/U_{\tau_0}$ Normalization of these profiles by the local U_τ enforces similarity in the inner region between the cases while causing a vertical shift (denoted by ΔB) in the logarithmic layer, which is correlated to the degree of DR [6]. For instance, the complete collapse of the nonactuated and actuated profiles over the first belt [Fig. 6(a)] suggests negligible DR at $x/\lambda_x = 0.125$. However, a monotonic increase in ΔB, i.e., increase in DR, can be observed with further downstream evolution. The drag changes particularly rapidly across the streamwise region: $0.375 \leqslant x/\lambda_x \leqslant 1.125$ [Figs. 6(b)–6(e)], after which it tends to nominally saturate to a steady state level. These characteristics align with the literature [26,31], wherein an initial streamwise transient is expected before the mean drag and turbulence flow statistics saturate/fully develop. The profiles also provide the reader with a qualitative sense of the accuracy of the modified composite fit, which underlines the upcoming discussion on the nominal streamwise variation of C_f.

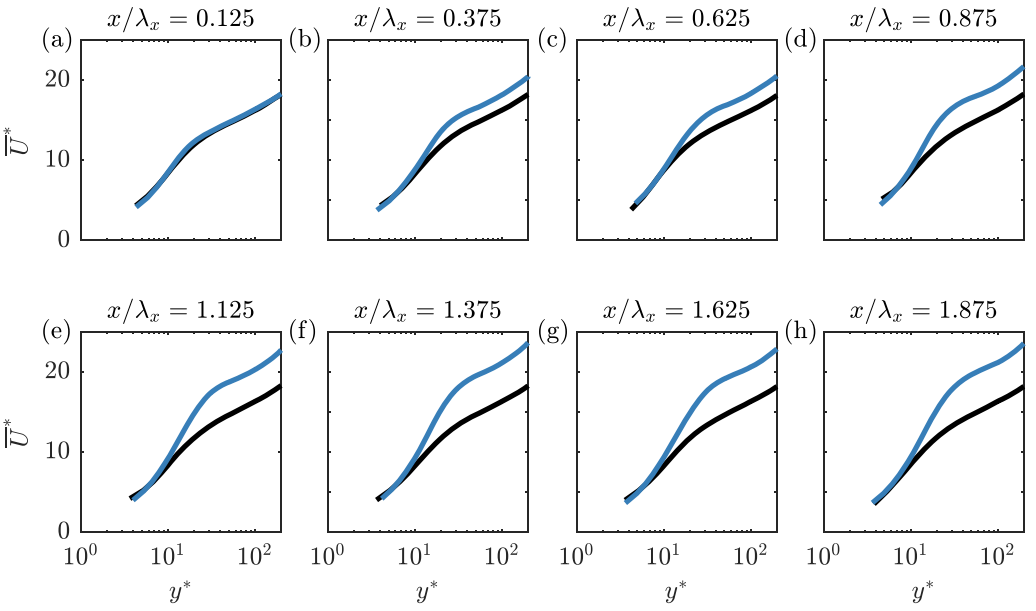

FIG. 6. Downstream evolution of the mean velocity profile, following the onset of actuation. Comparing the nonactuated (in black) and actuated case ($\lambda_x^+ = 942$ and $A^+ = 12$; in blue). Panels (a)–(h) correspond to the profiles over the respective belts no. 1–8 from FOV1.

We compare the skin-friction coefficient for the SqW and the nonactuated cases in Fig. 7(a) to quantify the rate of saturation of the drag modification. Here we derive the nominal C_f from the local values of U_τ used for the scaling in Fig. 6, based on the modified composite fit procedure (Appendix A). In line with the aforementioned behavior of the mean velocity profiles in Fig. 6, C_f rapidly attenuates across the interval $x \lesssim 1.5\lambda_x \sim 1.45\delta_0$, after which it tends to saturate to a new reduced state. We note a nominal DR $\sim$30% at $x \sim 1.45\delta_0$, suggesting that the TBL undergoes a further slow modification as it approaches the downstream eight belts (FOV2; $9.7 \lesssim x/\delta_0 \lesssim 11.7$), where a nominal DR $\sim$ 38% is obtained (see Sec. III E).

Investigation of the streamwise evolution of C_f is supported by the analysis of the turbulence statistics in the overlying TBL, for which we consider contours of $\overline{uu}^+$ and $-\overline{uv}^+$ in the x-y plane from FOV1 [Figs. 7(b)–7(e)], scaling the streamwise coordinate with λ_x. Note that, for this case, the wavelength is almost the same as the BL thickness; hence, scaling with these is interchangeable. To enhance legibility without influencing the conclusions, a smoothening was applied to the statistical contours (also repeated later in Fig. 11). For this, a Gaussian kernel was chosen to preserve sharp features, with the images convolved using 9- and 15-pixel kernels for the two stresses, respectively. Note that both these Reynolds stresses as well as wall-normal distances are normalized by $U_{\tau 0}$, and hence this figure allows differences between actuated and nonactuated cases in the "absolute" sense to be appreciated [22,25,26]. White lines with "+" markers indicate wall-normal location of the peak of $\overline{uu}^+$ in Fig. 7(b), while they indicate $y^+ = 15$ in Fig. 7(d), both of which are contours associated with the actuated case, $\lambda_x^+ = 942$. The magnitudes of $\overline{uu}^+$ and $-\overline{uv}^+$ at these locations are plotted in Figs. 7(c) and 7(e) respectively, for visualizing the spatial modifications of the near-optimal actuated case (in blue) against the nonactuated case (in black). As remarked previously in Sec. II A, the near-wall statistics display some spatial modulation, which is related to the actuation surface's imperfections; however, these do not essentially affect our conclusions. It can be observed that the peak in $\overline{uu}^+$ is attenuated by $\sim$40% and shifted to a higher wall-normal location almost immediately, already over the first belt [Figs. 7(b) and 7(c)]. The same can be noted for $-\overline{uv}^+$ in Figs. 7(d) and 7(e), which drops much more rapidly by $\sim 75 - 80\%$ within $\sim 0.1\delta_0$. This strong

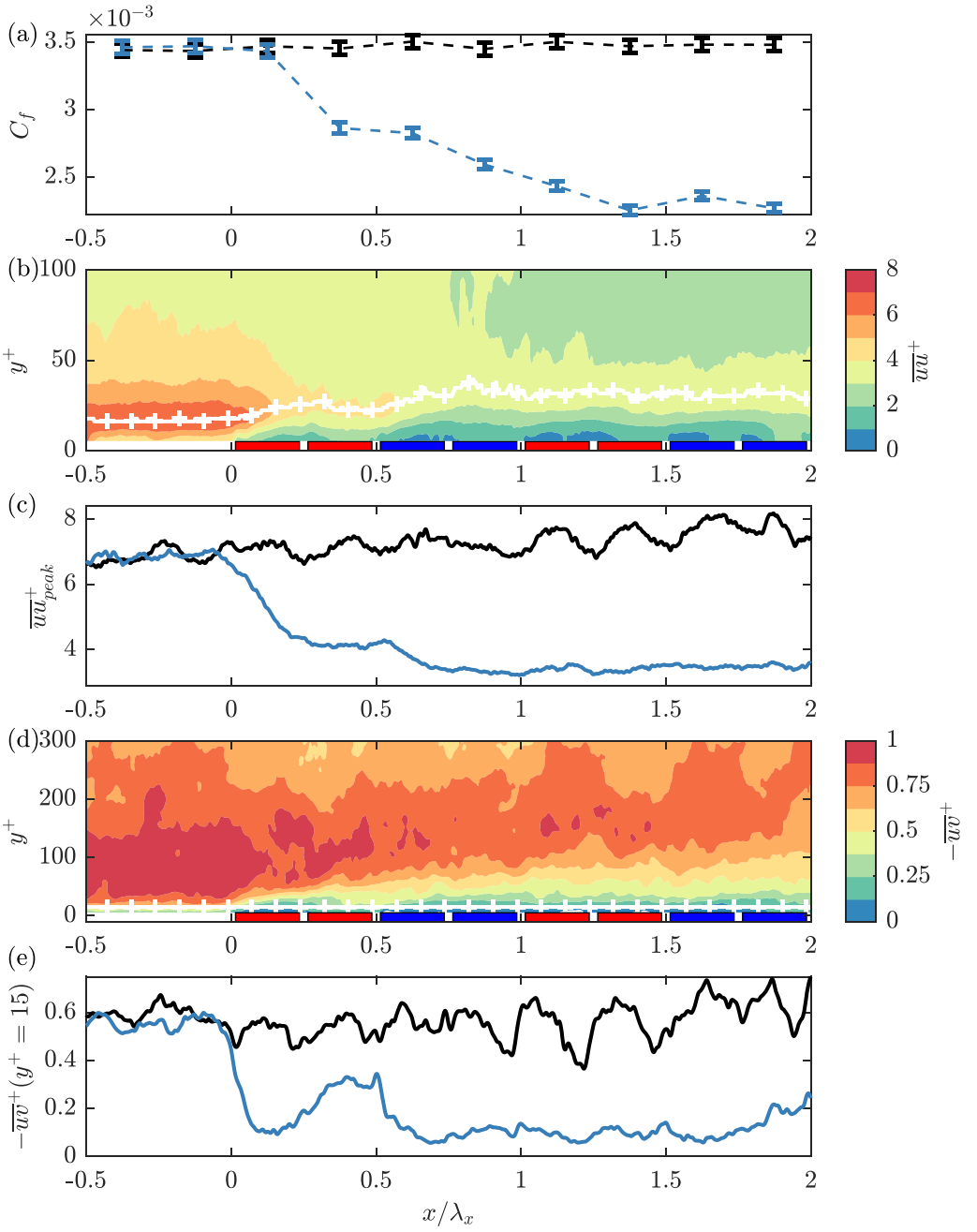

FIG. 7. Streamwise evolution of (a) skin-friction coefficient (C_f), only the markers corresponding to data and dashed lines are added for interpretability, and streamwise-wall-normal contours of (b) $\overline{uu}^+$ and (d) $-\overline{uv}^+$ for spatial forcing of $\lambda_x^+ = 942$ and $A^+ = 12.0$, attained from FOV1. The streamwise coordinate is scaled with λ_x under the current conditions $\lambda_x \sim \delta_0$. White "+" markers in (b) and (d), respectively, correspond to the line plots in (c) and (e), which compare $\overline{uu}^+$ and $-\overline{uv}^+$ between the actuated (in blue) and nonactuated case (in black). "+" marker in (c) corresponds to location of the near-wall peak in $\overline{uu}^+$, while that in (e) is fixed at $y^+ = 15$. Alike to Fig. 4, the shaded red (blue) regions denote the belts' location and positive (negative) spanwise motion direction, as such identifying the regions of forcing reversal.

attenuation signifies the dampening of the near-wall velocity streaks ($\overline{uu}^+$) that are inherently linked to the Reynolds shear-stress-producing events and, thereby, to the wall-shear stress [30,49]. Along with the "quick" (i.e., on short length scales) response, we can observe a more gradual attenuation in $-\overline{uv}^+$ that propagates deeper into the logarithmic layer (to beyond $y^+ > 300$), over a much larger streamwise extent covering at least the current FOV $x/\delta_0 \gtrsim 2$. This is a trend that qualitatively aligns with the established evolution of C_f.

Interestingly, however, as the TBL further evolves, both Reynolds stresses in the near-wall region start recovering to higher turbulence intensities as the TBL evolves towards the half-phase ($x \sim 0.5\lambda_x$). While this recovery is relatively minor for $\overline{uu}^+$ and effectively "plateaus," it is significant and clearly noticeable for $-\overline{uv}^+$. In contrast to $\overline{uu}^+$, the Reynolds shear stress is dominated by relatively small spatial and temporal scales, owing to which the latter responds more "quickly" to changes in the wall actuation condition [50]. This plausibly explains the differences between the spatial responses of the two stress components evident in Fig. 7. For completeness, we make a note here that contours of $\overline{vv}^+$ are dominated by similar scales as to $-\overline{uv}^+$ motions, and we have avoided showing them here for brevity (all available Reynolds stress contours are provided in a supplementary dataset; see details in the data availability section).

We further investigate the recovery within the forcing phase (i.e., intraphase recovery) by considering also the other two wavelength cases, $\lambda_x^+ = 471$ and 1884 (i.e., $0.5\delta_0$ and $2\delta_0$, respectively). Figure 8 presents the spatial evolution of C_f, and the line plots of the Reynolds stresses at similar y^+ locations as in Fig. 7, but now for all three cases. Note that in this figure, the x coordinate is scaled with δ_0, to better compare the development in physical distance, irrespective of the forcing wavelength. Figure 8(b) confirms that the recovery of $\overline{uu}^+$, which was only weakly apparent in Fig. 7(c), is indeed physical and is much more clearly evident when imposing a larger $\lambda_x^+ = 1884$ (in red). Both $\overline{uu}^+$ and $-\overline{uv}^+$ get "reattenuated" at their half-phase location ($x \sim 0.5\lambda_x$) for all cases, where the actuation initially changes forcing direction (i.e., $x/\delta_0 \lesssim 0.25$, $x/\delta_0 \lesssim 0.5$, and $x/\delta_0 \lesssim 1$ for $\lambda_x^+ = 471$, 942, and 1884, respectively) Notably, we can observe a strong similarity in the manner in which stresses react to the initial forcing input, regardless of wavelength, before the reversal in the wall-forcing direction occurs. Following its initial transient, the two cases for $\lambda_x^+ \lesssim 1000$, start to establish a quasi-streamwise-homogeneous response, while the postoptimal exhibits a strong phasewise variation. Such a streamwise alternate variation between attenuation and recovery continues to be maintained further downstream, even when the forcing is fully established, which we detail further in Sec. III D.

Assessing the skin-friction evolution in Fig. 8(a), it is worth highlighting that even though the established DR for the cases $\lambda_x^+ = 471$ and 942 have a significant difference in magnitude (see Sec. III E), their initial spatial development ($x/\delta_0 \lesssim 0.5$) is very similar. In fact, the C_f trend for both these cases follows a similar response to the oscillating-wall experiment ($T^+ = 67$, $A^+ = 11.3$) of Ricco and Wu [23] (in gray circles), hinting at universality in the initial TBL response for suboptimal and near-optimal cases.

We find that for the postoptimal case ($\lambda_x^+ = 1884$), and initially also the near-optimum case ($\lambda_x^+ = 942$), an interesting phenomenon occurs; namely, the response of C_f and turbulence recovery are notably out-of-phase. Over the first half-phase (i.e., $x < \lambda_x/2$), the skin friction reflects a monotonic decline while both $\overline{uu}^+$ and $-\overline{uv}^+$ display a significant recovery. Moreover, once the reversal of the forcing direction occurs for the postoptimal case, C_f actually increases while $-\overline{uv}^+$ reveals a strong attenuation, similar to the one at initial forcing ($x = 0$).

Based on these findings, we can conclude that the majority of the flow transient for the (sub)optimal cases occurs within $x/\delta_0 \lesssim 1$, after which there is only minor streamwise variation before the fully established control regime is attained (see further discussion in Sec. III D). Hereby, we find that the present scaling of the streamwise transient with δ_0 is consistent with the available literature, which shows that the transient behavior is insensitive to the actuation parameters as well as the Reynolds number (noted previously in [13,51]). Our findings for postoptimal wavelengths reflect a significant attenuation of turbulence activity, followed by its intraphase recovery, in

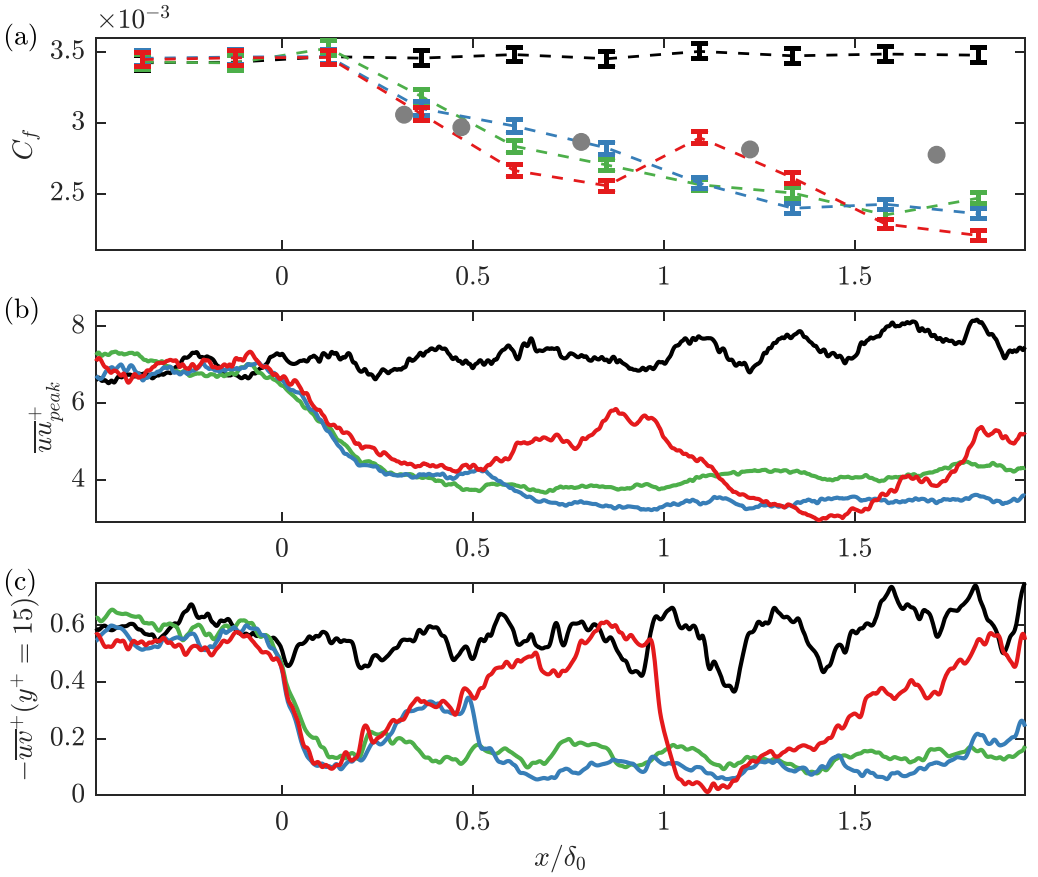

FIG. 8. Streamwise evolution of (a) skin-friction coefficient (C_f), note only the markers correspond to data; dashed lines are added for interpretability, (b) $\overline{uu}^+$ and (c) $-\overline{uv}^+$ for wavelengths $\lambda_x^+ = 471$ (green line), 942 (blue line), 1884 (red line) at $A^+ = 12.0$, and the nonactuated reference (black line), at the initiation of actuation (FOV1). In (a), the gray dotted markers indicate DR evolution of Ricco and Wu [23]; skin friction was obtained following $C_f = C_{f0}(1 - \mathrm{DR}/100)$, with C_{f0} used of the current study. The line plots correspond to the Reynolds stress at (b) the near-wall peak in $\overline{uu}^+$, while that in (c) is fixed at $y^+ = 15$.

the initial and latter parts of the half-phase, respectively. Notably, we found that the intraphase turbulence recovery and skin-friction evolution are strongly out-of-phase. We aim to reconcile and discuss these findings more elaborately in Sec. III C after we establish the associated phasewise variations of the Stokes strain rate for SqW forcings in Sec. III B (as previously established for SinW forcings in Sec. I A).

B. Distinguishing Stokes strain between sinusoidal and square-wave forcing

This subsection draws inspiration from the previous studies of Leschziner and co-workers [24–26] by determining the Stokes strain and the Stokes strain rate (SSR) for the SqW, in comparison to the SinW. By qualitatively contrasting the characteristic SSR responses, we aim to further elucidate the observed different regimes of attenuation and recovery of turbulence over the half-phase of SqW wall-forcing (see Sec. III A). These studies were reviewed in Sec. I A and describe the correlation between the occurrence of high SSR and near-zero SSR (i.e., constant "lingering" Stokes strain) with turbulence attenuation and its recovery, respectively. Although these

past works were focused on temporal SinW forcings, where the SSR is defined as $\partial^2\widetilde{W}/\partial t\,\partial y$, it is reasonable to conjecture that their findings also extend to spatial SinW forcing [10,11], for which equivalently the SSR would be defined by $\partial^2\widetilde{W}/\partial x\partial y$.

For the present discussion, we have chosen to deploy the modified spatial Stokes layer (SSL) model, considering unitary A^+ (note that the results are linear in A), which has been previously reported and validated using experimental data in Knoop *et al.* [21] and also discussed summarized in Appendix B for completeness. The choice for using the validated SSL model was made in view of (i) the absence of stereoscopic PIV data required to compute the SSR directly and (ii) the large uncertainties associated with the estimation of spatial gradients (especially second derivatives owing to measurement noise), even if stereo-PIV were conducted. The spatial wave characteristics for the modified SSL are selected to match the optimum DR case of $\lambda_x^+ = 942$. For this, we have verified that the 2 mm "static" regions between belts with the same W_w sign do not significantly alter the global response [21], and hence we have excluded this detail from the model for purposes of simplification, and treat adjacent belts running in the same direction as a single belt (further discussion to justify this approximation can be found in Appendix B). Figures 9(a) and 9(b) present the analytically obtained Stokes layer forcings ($\widetilde{W}$) for SinW (left) and SqW (right) scenarios across a single phase ($0 \leqslant x \leqslant \lambda_x$). For reference, a three-dimensional representation of the SinW scenario was presented previously in Fig. 3. The differences between SqW and SinW forcings can be clearly observed in the near-wall region, with the former having constant spanwise wall velocity magnitudes, except near $0.5\lambda_x$ and λ_x, which mark the location between the counter-running belts. However, the two strategies exhibit much more similar $\widetilde{W}^+$ behavior further away from the wall, likely due to the viscous diffusion effects.

Next, we compare the Stokes strain ($\partial\widetilde{W}/\partial y$) contours in Figs. 9(c) and 9(d) to the spanwise velocity contours. In the case of SinW forcing, the maximum Stokes strain region precedes the location of maximum spanwise velocities, $x/\lambda_x = 0.25$ and 0.75, by about one-eighth of the phase. In contrast, the highest amplitudes of $\partial\widetilde{W}/\partial y$ for SqW forcing are obtained immediately downstream of the switch in the sign of W_w. We denote the location of the wall-based Stokes strain maxima by the dashed vertical lines, in the respective plots for SinW and SqW. The differences between $\partial\widetilde{W}/\partial y$ for SqW and SinW forcings are also compared quantitatively via a line plot at $y^+ = 5$ in Fig. 9(g). The peak magnitude for the SqW is nearly 1.5 times higher than for SinW (assuming the same forcing amplitude), and the aforementioned differences in phasewise location of the peak strain are also evident. However, we observe a similar response between the two forcing types further away from the wall, which is confirmed by the line plot at $y^+ = 15$ Fig. 9(h).

This paves the way for investigating the SSR, which has been described as key to enforcing drag reduction within a forcing phase (refer to Sec. I A). By generalizing from the findings of Agostini and co-workers [24–26], we pose the hypothesis that upon the imposition of high SSR, the turbulence is strongly attenuated, while an extended fetch of lingering Stokes strain can be associated with the recovery of turbulence. As illustrated in Figs. 9(e) and 9(f) for SinW and SqW forcings, regions of elevated SSR magnitude correspond to the phases associated with a switch in the sign of $\widetilde{W}$, thereby occurring twice per period. However, the SSR is very small in the domain of maximum strain for SinW forcing, i.e., the strain lingers at a relatively low level in this region. The qualitative response for the SqW forcing, however, is markedly different. The forcing is observed to be much stronger and is primarily "localized" to the region associated with a switch in the sign of $\widetilde{W}$ (i.e., forcing direction reversal). Hence, the dominant forcing term is strong and impulsive rather than the gradual variation noted in the case of SinW, which is reflected quantitatively in Figs. 9((i) and 9(j). The peak SSR magnitude for SqW forcing is over 12 times stronger than that for SinW at $y^+ = 5$. This suggests that the local forcing experienced by the flow, which is responsible for attenuating the self-sustaining near-wall cycle, is one order stronger for the SqW than for the SinW. Note, however, that this does not linearly correlate to DR, per its saturation under high amplitudes of forcing [53]. Downstream of the high SSR forcing, the rest of the half-phase is characterized by lingering Stokes strain, i.e., near-zero SSR. In Sec. III C we aim to associate these SqW-specific

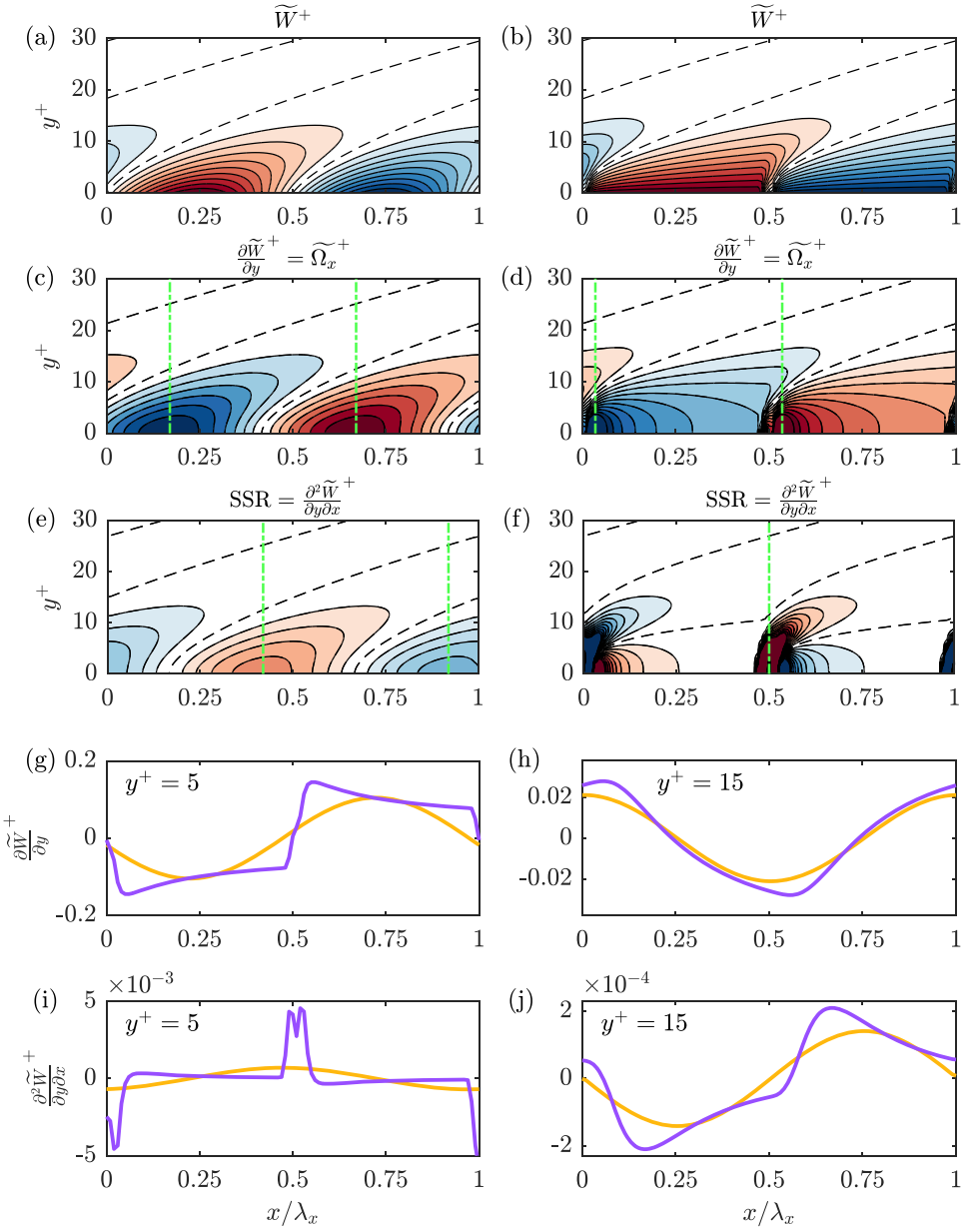

FIG. 9. Phasewise contours of the analytical solution for the (modified) Stokes layer for (a), (c), (e) SinW [52] and (b), (d), (f) SqW forcing [21]. (a), (b) Spanwise velocity, contour level range: $-1{:}0.1{:}1$; (c), (d) Stokes strain, $\partial\widetilde{W}^+/\partial y$ contour level range: $-0.2{:}0.02{:}0.2$; (e), (f) Stokes strain rate, $\partial^2\widetilde{W}^+/\partial x\partial y$ contour level range: $-0.002{:}2 \times 10^{-4}{:}0.002$. Vertical green dash-dotted lines in (c)–(f) denote the locations of the respective wall-based peak magnitudes. We contrast the SinW (orange) and the SqW (purple) forcings by their respective (g), (h) Stokes strain and (i), (j) SSR, at (g), (i) $y^+ = 5$ and (h), (j) $y^+ = 15$.

SSR characteristics directly with the response of turbulence (recovery), while we speculate plausible reasons for the out-of-phase behavior noted for the skin friction.

C. Distinguishing the response of turbulence and skin friction to square-wave forcing

From our previous discussion, we can establish that the SqW has two clearly distinguishable regions of SSR within a half-phase ($\lambda_x/2$): subphase I of high impulsive SSR associated with the reversal of forcing direction, followed by a subphase II characterized by an extended domain of lingering Stokes strain (i.e., negligible SSR) owing to constant W_w. Here we define subphases I and II based on the SSR at the wall to be significant and near-zero, respectively, which subsequently determines their streamwise fetch. Based on our analytical assessment of the near-optimum wavelength in Fig. 9, both subphases span approximately half of the half-phase (i.e., $\lambda_x/4$). As a result of the SqW-type boundary condition, the extent and SSR magnitude of subphase I is largely invariant with λ_x. In contrast, the fetch of lingering Stokes strain of subphase II extends in proportion to the wavelength. In this section we aim to reconcile these two SSR subphases with the response of turbulence observed in Sec. III A. We also distinguish between the response of the turbulence and the friction drag to wall-forcing.

The starting point for our discussion is the streamwise-wall-normal contour of $-\overline{uv}^+$, at the initiation of forcing, where the intraphase recovery is most pronounced. The choice for considering the Reynolds shear stress was motivated by its link to C_f through a (weighted) wall-normal integration across the boundary layer [54,55]. We report this through colored contours for all three λ_x^+ cases in Figs. 10(a)–10(c). To facilitate the discussion on variation in intraphase recovery with λ_x^+, we highlight three constant energy contour levels, $-\overline{uv}^+ = [0.25\ 0.55\ 0.75]$, which are subsequently overlaid in Fig. 10(d) to compare and contrast their streamwise evolution. In the streamwise direction, an upward movement of the contours is representative of attenuation, while its movement toward the wall can be associated with turbulence recovery. Upon initial imposition of forcing at $x = 0$, the aforementioned gradual streamwise evolution of an attenuated $-\overline{uv}^+$ state, penetrating high into the boundary layer to over $y^+ > 300$ [see Fig. 7(d)], is reflected among all cases. This response suggests that the impulsive forcing generates an energy-attenuated internal boundary layer that subsequently propagates into the existing TBL, and through which it adapts to the new low-energy near-wall state initiated by the high SSR forcing. Its streamwise evolution is best reflected by the collapse of the $-\overline{uv}^+ = 0.75$ contour for all cases throughout the considered streamwise extent. Initially, for $x/\delta_0 \lesssim 0.5$, this similarity is also reflected in the $-\overline{uv}^+ = 0.55$ contour, after which the postoptimal case recovers, while the behavior of the two $\lambda_x^+ \lesssim 1000$ cases stay similar throughout the streamwise extent. As such, we propose, distilled from our experimental results, that an SSR forcing "event" during subphase I carries with it a certain streamwise domain of influence, which extends significantly beyond the fetch of subphase I, governed by a long-length scale of order δ_0 (linked to the wall-normal propagation of the shear-stress attenuated state). This trend is consistent with the δ_0 scaling that we established for the evolution of C_f upon initial forcing [Fig. 8(a)].

The significant intraphase recovery observed in the case of $\lambda_x^+ = 1884$, best characterized by the $-\overline{uv}^+ = 0.25$ and 0.55 contours, remains confined to the near-wall region ($y^+ \lesssim 75$) and can be associated with the lingering Stokes strain in the extended half-phase of constant W_w. When the forcing direction reverses at $x/\delta_0 \sim 1$, and SSR is imposed again, a strong attenuation and a similar recovery region can be observed, emerging over the downstream region of the second half-phase. This recovery phenomenon is suggested to be governed by a relatively smaller length scale as compared to the hypothesized δ_0 for C_f, owing to the fact that it is established within the waveform. With reference to the vortex tilting mechanism of Agostini *et al.* [25], this phenomenon is likely to be linked to the recovery time of the streaks of approximately $t^+ \sim 50$ [56], which converts to a length scale of $\mathcal{L}^+ \approx \mathcal{U}_c^+ t^+ \sim 500$ considering the well-accepted near-wall convection velocity $\mathcal{U}_c^+ \sim 10$. This likely explains the observation of a significant intraphase recovery notably for the postoptimal case, where the half-phase extends far beyond $\lambda_x^+/2 \gg 500$.

Based on this, we can hypothesize the wavelength-dependent response of the TBL as resulting from a balance between having a sufficient fetch for subphase I forcing effect to establish its full potential, while limiting at the same time the intraphase recovery associated with an extended

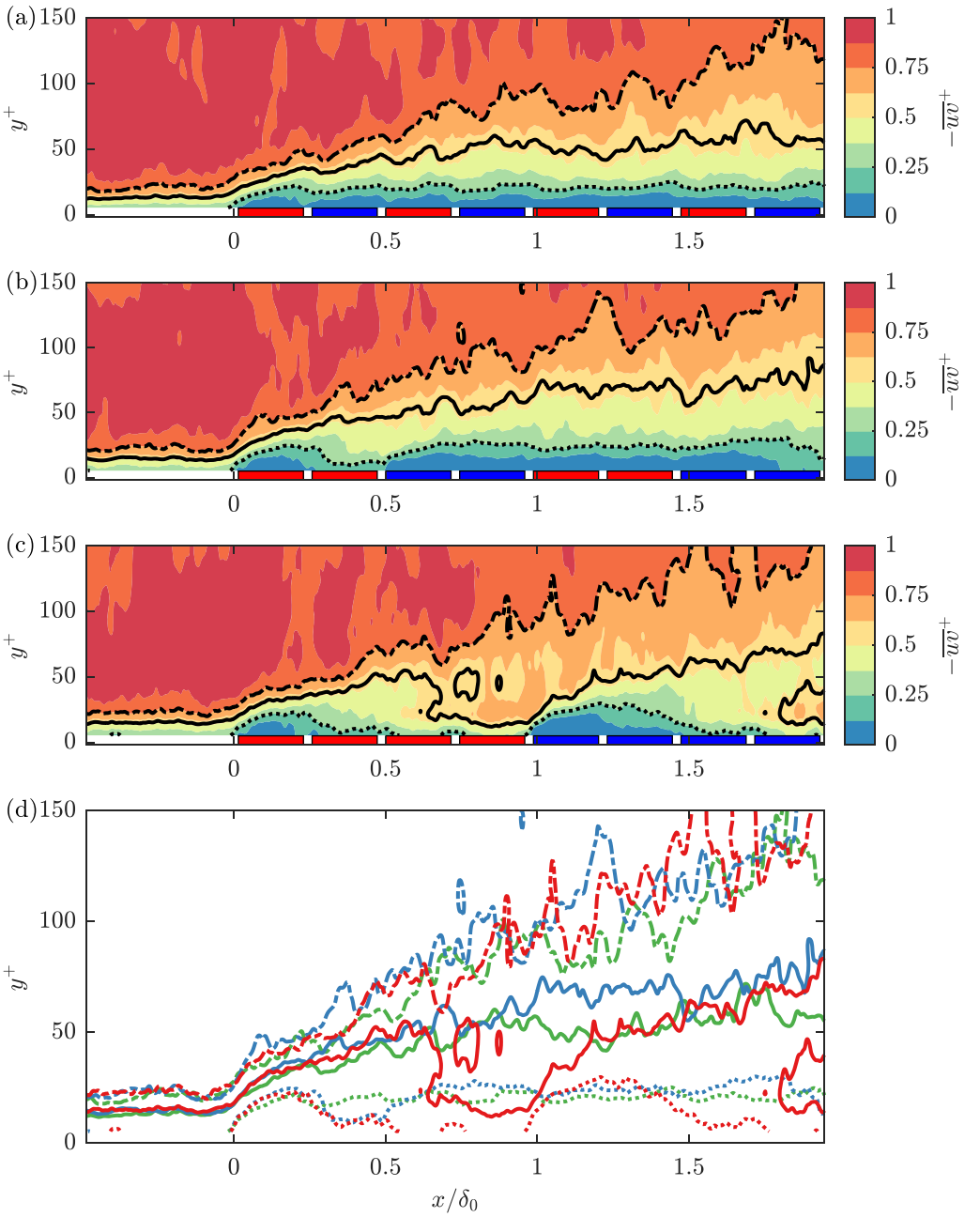

FIG. 10. Streamwise evolution of $-\overline{uv}^+$ in the streamwise-wall-normal plane at the initiation of forcing (FOV1), for wavelengths (a) $\lambda_x^+ = 471$ (green), (b) 942 (blue), and (c) 1884 (red) at $A^+ = 12.0$. Panel (d) presents a comparison of the black contour lines in (a)–(c) that denote $-\overline{uv}^+ = [0.25\ 0.55\ 0.75]$ (dotted, solid, dashed). Note the change in the limits of the wall-normal extent to $y^+ = [0,\ 150]$. Alike to Fig. 4, the shaded red (blue) regions denote the belts' location and positive (negative) spanwise motion direction, as such identifying the regions of forcing reversal.

subphase II. Attesting to this, in Fig. 8(b) the suboptimal forcing, with only a limited fetch between the respective subphase I forcings, attains a less-attenuated state of the streamwise stress peak (representative of the turbulent streaks), compared to the near-optimum, whereas the postoptimal case reflects a significant intraphase recovery of the turbulent streaks as subphase II extends significantly beyond $\mathcal{L}^+ \gg 500$.

Next, we associate the response of C_f with the characteristic SSR subphases, particularly for the postoptimal case, which is characterized by a marked out-of-phase response between C_f and the recovering turbulence. Note that the present PIV experimental data do not provide enough fidelity to investigate the DR mechanisms through an energy or enstrophy budget analysis considered in Refs. [25,26,34]. Hence, here we focus on comparing the response of C_f relative to the SSR and attempt to reconcile present findings with the literature. A detailed examination of Agostini *et al.* [25] reveals a similar out-of-phase pattern to our experiment, with C_f locally increasing when SSR is high (i.e., subphase I) followed by its subsequent decline as the stokes strain lingers (i.e., subphase II). Inferring from our earlier experimental observations, the latter trend may plausibly be explained by the differences in the streamwise extent over which the two phenomena respond. Specifically, we conjecture that the δ_0-scaled behavior of decreasing C_f leads to a gradual decrease over the half-phase in response to the preceding subphase I forcing, owing to the wall-normal propagation of an attenuated $-\overline{uv}^+$ internal boundary layer. Concurrent is the emergence of turbulence recovery, which takes place predominantly in the near-wall region $y^+ \lesssim 50$, thereby contributing only minimally to the enhancement of C_f. For scrutiny, we have verified that the $y^+ > 50$ region contributes on the order of ∼80%–90% to the Reynolds shear stress integral of both the Fukagata *et al.* [54] and Elnahhas and Johnson [55] identities [regardless of the $(1 - y/\delta)$ weighting for the former]. However, the intraphase recovery is believed to exert a more pronounced effect on the marked increase in C_f during subphase I, which will be addressed in the subsequent discussion. We aim to substantiate this phenomenon by referring back to the earlier introduced (refer to Sec. I A) vortex-tilting/stretching mechanism by Agostini *et al.* [25]. As noted by Umair and Tardu [34], the SSR-induced tilting of the near-wall turbulent streaks is associated with a localized increase in C_f. Therefore, a greater recovery of the streaks leads to a significantly higher local increase in C_f. Our experimental data in Fig. 8(b) supports this interpretation. The streamwise Reynolds stress peak, characteristic of these streaks, shows significant reestablishment near the end of the half-phase ($0.5 \lesssim x/\delta_0 \lesssim 1$). At $x/\delta_0 \sim 1$, the subsequent application of high SSR in subphase I induces tilting of these partially recovered streaks. Hence, this out-of-phase C_f behavior becomes distinctly observable only under postoptimal conditions, where substantial streak recovery occurs during the lingering half-phase. These characteristic phenomena become more clearly evident when the wall-forcing has fully established, which we will discuss next in Sec. III D.

D. Streamwise evolution of turbulence statistics under fully established forcing

In this section we examine the TBL response under fully established forcing conditions, further substantiating the previously discussed flow mechanics (Sec. III C). We are now concerned with the flow field over the most downstream region of the actuation domain (covering belts no. 40–48), in FOV2. As becomes evident from Fig. 11, which presents the streamwise variation of C_f, $\overline{uu}^+$, and $-\overline{uv}^+$. A fully developed regime is attained (i.e., no global spatial transient) for all three cases, while, at the same time, the postoptimal case still exhibits strong intraphase variations.

Assessing the spatial variation of skin friction in Fig. 11(a) confirms streamwise homogeneous behavior for $\lambda_x^+ = 471$ and 942, owing to the physically small streamwise spacing between the subsequent SSR forcing events (i.e., the half phase extends only $\lambda_x^+/2 \leqslant 500$), thereby not permitting significant recovery. A similar effect is noted for both these cases in terms of the streamwise Reynolds stress [Fig. 11(b) and 11(c)], with the peak value location at $y^+ \approx 25$–30 relative to $y^+ \approx 15$ for the uncontrolled case [see also Fig. 5(b)]. However, the turbulence attenuation is observed to be strongest for the optimum wavelength case. Accordingly, and in line with the available literature [5,10], the near-optimum case ($\lambda_x^+ = 942$) outperforms the $\lambda_x^+ = 471$ case also in

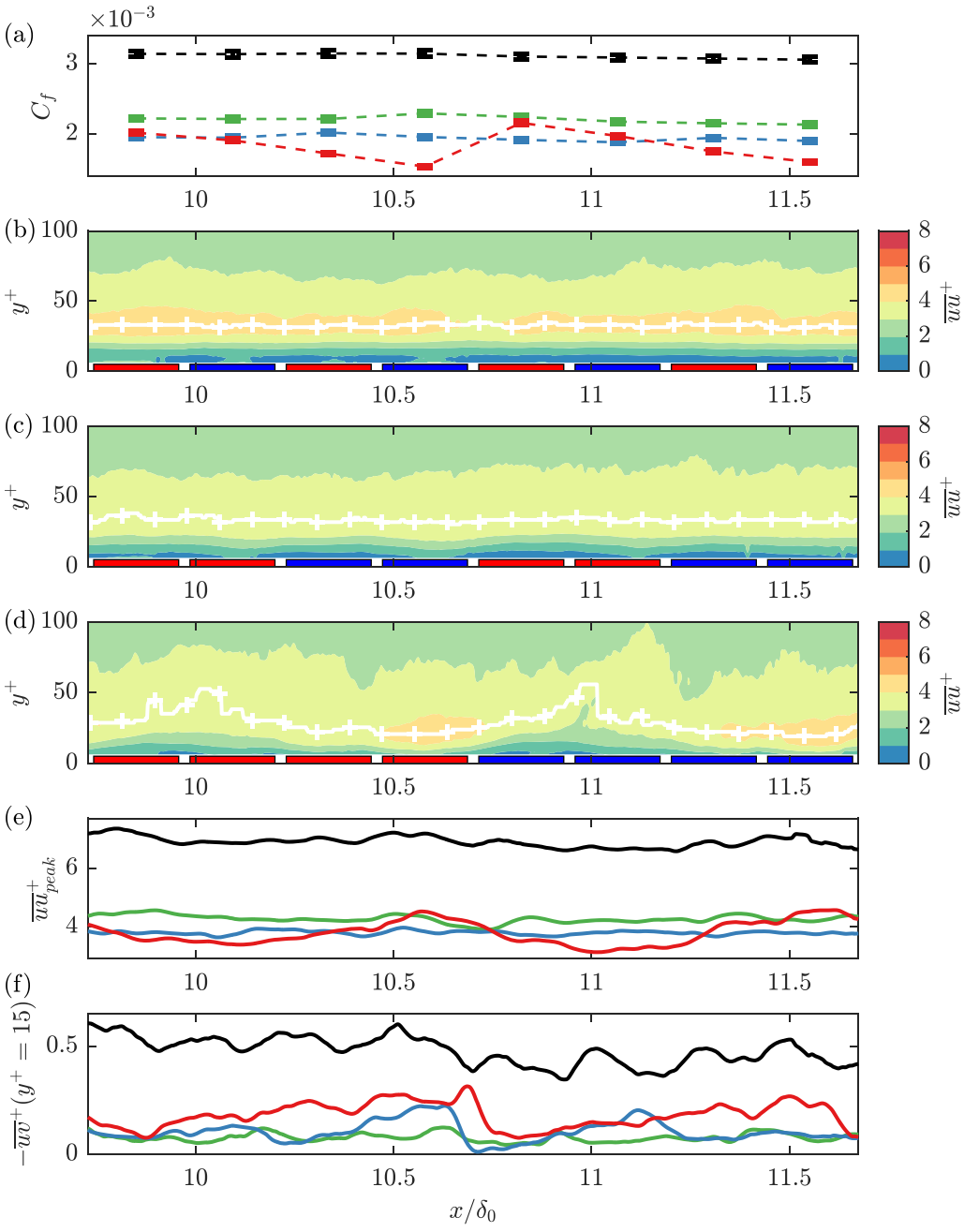

FIG. 11. Streamwise evolution of (a) skin-friction coefficient (C_f), note only the markers correspond to data; dashed lines are added for interpretability, (b)–(d) streamwise-wall-normal contours of $\overline{uu}^+$, for wavelengths $\lambda_x^+ = 471$ (green), 942 (blue), 1884 (red) at $A^+ = 12.0$, and the nonactuated reference (black), towards the downstream end of forcing as obtained from FOV2. Similar to Fig. 7, the line plots in (e) and (f) correspond to the magnitude of the near-wall peak in $\overline{uu}^+$ [denoted by white "+" markers in (b)–(d)], and $-\overline{uv}^+$ at $y^+ = 15$, respectively. Alike to Fig. 4, the shaded red (blue) regions denote the belts' location and positive (negative) spanwise motion direction, as such identifying the regions of forcing reversal.

terms of skin-friction reduction [Fig. 11(a)]. The established C_f of both these actuated cases, relative to the nonactuated reference, reflects an integral DR $\sim$32% and $\sim$38%, respectively (discussed elaborately in Sec. III E).

In accordance with the phenomenology discussed in Sec. III C, the postoptimal case at $\lambda_x^+ = 1884$ (in red) reflects a qualitatively similar response, however, now fully established. Upon the imposition of high SSR where forcing reversal occurs (most upstream and halfway through the FOV), the turbulent stresses are attenuated [Figs. 11(d)–11(f)]. Subsequently, when the SSR lingers in subphase II, turbulence recovery occurs, which is gradual for $\overline{uu}^+$ as compared to a relatively more impulsive response of $-\overline{uv}^+$. Note that the magnitude of the intraphase variation is not as high as in FOV1, likely owing to the TBL's overall energy-reduced state. We also reaffirm the out-of-phase response of C_f to the turbulence over the half-phase where W_w is constant (subphase II). Here C_f is continually declining, whereas a local increase is observed upon reversal of forcing direction (i.e., high SSR, subphase I). This is supportive of our previously introduced inference that C_f attenuates in response to the high SSR forcing over a longer spatial extent, while at the same time, the near-wall turbulence already recovers when the Stokes strain lingers. Representative of the turbulent streaks, the streamwise stress peak in Figs. 11(d) and 11(e) exhibits significant phasewise variations in magnitude, ranging between $\overline{uu}^+_{\text{peak}} = 3.4$–$4.5$, and wall-normal location between $y^+ \sim 25$–50. The reestablishment of $\overline{uu}^+$ toward the end of the half-phase, at $x/\delta_0 \sim 10.5$, and 11.5, is supportive of the SSR vortex-tilting mechanism to locally increase C_f (discussed previously in Sec. III C).

To summarize, we have shown that the turbulence response in the fully established state is self-consistent with the previously discussed phenomenology in the initial transient region (Sec. III C), which was associated with individual SSR subphases. A conceptual synthesis of the interpretation of these results will be presented and discussed in Sec. IV after we elaborate on the integral performance parameters of the SqW-type forcing in Sec. III E.

E. Turbulent drag reduction via steady spatial square-waves of spanwise velocity

To conclude our discussion of the results, this subsection establishes the integral flow control potential of the SqW forcing imposed experimentally at $\text{Re}_\tau = 960$, for varying forcing wavelengths (Table I). A combination of ensemble as well as streamwise averaging is applied to the streamwise velocity profiles over the last eight belts in FOV2 ($\langle\overline{U}\rangle_x$), and they are plotted after normalizing with the reference (nonactuated) friction velocity ($U_{\tau 0}$) in Fig. 12(a). The profiles are averaged across four phases/forcing cycles (for $\lambda_x^+ = 471$; in green), two phases ($\lambda_x^+ = 942$; in blue), or a single phase ($\lambda_x^+ = 1884$; in red) depending on the spatial forcing wavelength. However, these differences do not influence the variations exhibited by the $\langle\overline{U}\rangle_x$ profiles owing to the fully established control effect and minimal spatial development of the TBL in this region (previously verified in Fig. 11). The profiles, however, would be influenced by the streamwise extent of turbulence attenuation and recovery within each forcing phase, which varies with λ_x^+.

In line with the literature [10,13], all $\langle\overline{U}\rangle_x^+$ profiles for actuated cases collapse in the far outer region and exhibit a notable downward shift in the viscous sublayer. The reduction of near-wall velocity is accompanied by an increase/overshoot of $\langle\overline{U}\rangle_x$ beyond $y^+ \geqslant 20$, which extends up to a wall-normal height of approximately $y^+ = 400$. This is a well-known feature [5,18,33] noted on imposition of spatiotemporal wall-forcing. Choi and Clayton [33] explained that this modification results from a resultant mean spanwise vorticity component, $\widetilde{\Omega}_z$, due to the periodic spanwise tilting of the $\widetilde{\Omega}_x$ component associated with the Stokes layer.

We next implement the modified composite fitting procedure discussed in Appendix A on the mean velocity profiles to estimate the nominal DR. Figure 12(b) depicts $\langle\overline{U}\rangle_x^*$ versus y^* for the same cases as in Fig. 12(a), but normalized by the actual U_τ estimated via the modified composite fit. While the collapse of all $\langle\overline{U}\rangle_x^*$ profiles in the near-wall region is enforced, the vertical offset of the actuated cases in the intermediate/log-region (denoted by ΔB) is a function of DR. As expected,

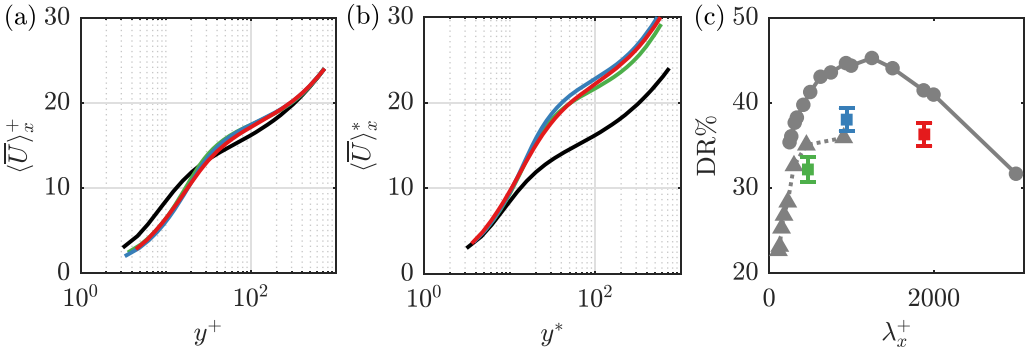

FIG. 12. (a), (b) Mean streamwise velocity profiles for wavelengths $\lambda_x^+ = 471$ (green), 942 (blue), 1884 (red) at $A^+ = 12.0$, and the nonactuated reference (black), normalized by flow properties associated with (a) nonactuated ($U_{\tau 0}$) and (b) actual (U_τ) flow conditions. (c) Drag reduction (DR%) as a function of λ_x^+ for the SqW forcing scenarios investigated experimentally (in colored symbols) at $A^+ = 12$. Also considered for comparison are DR% estimates from channel DNS considering SinW forcing: solid line, Viotti *et al.* [10] at $\mathrm{Re}_\tau = 200$, and dotted line, Gatti and Quadrio [6] at $\mathrm{Re}_\tau = 906$.

the $\langle\overline{U}\rangle_x^*$ profile associated with the $\lambda_x^+ \approx 1000$ case has the highest vertical offset among the three wall-forcing cases, suggesting the greatest DR. This is quantified in Fig. 12(c) depicting DR as a function of λ_x^+ for all three SqW forcing cases considered at $\mathrm{Re}_\tau = 960$. These estimates are compared against published results from the channel DNS of Viotti *et al.* [10] ($\mathrm{Re}_\tau = 200$; purely spatial wall-forcing) and Gatti and Quadrio [6] ($\mathrm{Re}_\tau = 950$; STW forcing at $\omega = 0$), both considering SinW forcing at $A^+ = 12$. A maximum DR ~38.1%, with a 95% confidence interval of ±1.31%, is found for the present experiments at $\lambda_x^+ = 942$, which compares well with DR noted for the optimum wavelength case in the literature [6,10,11]. In contrast, the sub- and postoptimal forcing cases have a DR of ~32.1 ± 1.44% and ~36.3 ± 1.35%, respectively. Further, the rate of variation of DR with λ_x^+ is consistent with the literature, with DR increasing rapidly for suboptimal wavelengths and decreasing gradually in the postoptimal region. The slightly higher DR noted for present experiments than DNS (for SinW), at comparable Re_τ [6], may be either owing to the overall greater efficacy of the SqW forcing than the SinW forcing as elucidate by Cimarelli *et al.* [57] for temporal forcing, or an artifact of the modified composite fit methodology. Nonetheless, the present focus is on obtaining the qualitative trend of DR% with λ_x^+ for SqW forcing, which is consistent with the literature.

Figure 13 presents wall-normal profiles of the streamwise and ensemble-averaged Reynolds stresses, scaled with either $U_{\tau 0}$ [Figs. 13(a) and 13(b)] or U_τ [Figs. 13(c) and 13(d)]. The near-wall peak in $\langle\overline{uu}\rangle_x$ plotted in Figs. 13(a) and 13(c) signifies the intensity of the near-wall velocity streaks and their self-sustaining cycle [58], while $-\langle\overline{uv}\rangle_x$ in Figs. 13(b) and 13(d) is considered in view of its analytical links with the wall-shear stress [55]. In general, all the actuated cases reveal a strong control effect represented by the attenuation of the Reynolds stresses in an absolute sense, with the near-wall $\langle\overline{uu}\rangle_x^+$ peak reducing by up to 47%. When normalizing with actual U_τ, we observe a slight increase in $\langle\overline{uu}\rangle_x^*$ and $-\langle\overline{uv}\rangle_x^*$ in the outer layer, which is consistent with the experimental findings of Chandran *et al.* [18] for STW forcing. For the two cases corresponding to $\lambda_x^+ \leqslant 1000$, the upward shift in the peak location for both $\langle\overline{uu}\rangle_x^+$ and $\langle\overline{uu}\rangle_x^*$ suggests the near-wall viscous cycle moves further away from the wall, causing the reduction in wall-shear stress [6,27]. Beyond the optimum wavelength, i.e., $\lambda_x^+ = 1884$, however, the near-wall $\langle\overline{uu}\rangle_x$ peak gets broader and moves closer to the wall again. This is likely an artifact of streamwise averaging across both—attenuated and recovering streamwise variance profiles—noted across two distinct portions over the forcing phase (Fig. 11). The same reasoning can be extended to explain the unconventional mean $\langle\overline{U}\rangle_x$ profile in the log region for $\lambda_x^+ = 1884$ case [Fig. 12(b)]. Similar modifications to the mean and

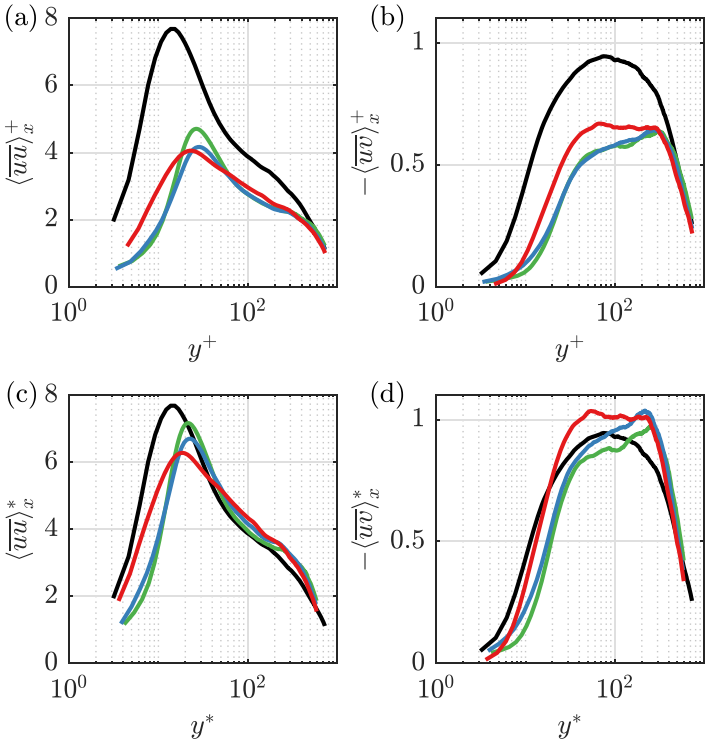

FIG. 13. Wall-normal profiles of turbulence statistics for varying λ_x^+: (a), (c) streamwise Reynolds stress and (b), (d) Reynolds shear stress, scaled with (a), (b) $U_{\tau 0}$ and (c), (d) U_τ, respectively. The line styles correspond to Fig. 12, and are also shown in Table I.

turbulent flow properties have been observed previously by Rouhi *et al.* [27] on imposition of STW forcings beyond optimal frequencies, but this study presents a phenomenological explanation for the same based on a phasewise variation of the SSR (i.e., DR mechanism).

IV. CONCEPTUAL SKETCH OF THE FLOW PHENOMENOLOGY AND DISCUSSION

Based on the experimental results documented in the preceding sections, we have established the impact of wavelength variation on the streamwise evolution of the turbulence modification and C_f for SqW forcing. Founded on the available literature [25,37], we hypothesized that the SSR-related turbulence modification for SinW could be extended to the SqW, linking high SSR and lingering Stokes strain to, respectively, turbulence attenuation and recovery. For the SqW specifically, the SSR can be clearly distinguished into two regimes: (a) subphase I of high and impulsive SSR that extends over a finite streamwise extent starting from the location of wall-forcing reversal (i.e., at $\lambda_x/2$) and quasi-independent of λ_x, and (b) subphase II associated with near-zero SSR owing to constant wall velocity, leading to its region of influence being proportional to λ_x. To clarify our observations, we present a conceptual sketch in Fig. 14 of the TBL-modifying phenomenology, where we distinguish the modification in terms of wavelength and waveform. We present this sketch to represent the situation at the initiation of forcing since the response is most pronounced here, while at the same time representative of the established dynamics that eventually emerge. Our findings reflected the initial turbulence attenuation to be similar over the first half-phase of forcing, $x/\lambda_x < 0.5$, for both the optimal and postoptimal cases as depicted in Figs. 14(a) and 14(b). Such a response may plausibly be attributed to the similarity of the initially imposed SSR. Subsequently, the optimal case

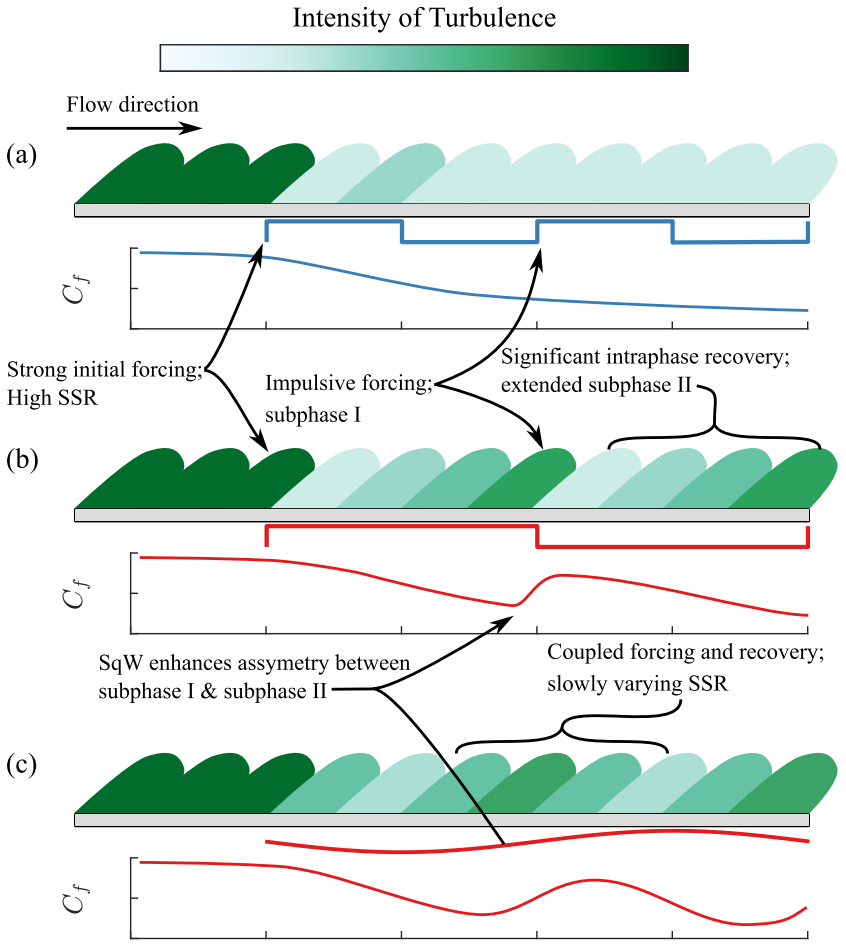

FIG. 14. Conceptual sketch of the phenomenology illustrated schematically through the Reynolds shear stress turbulence intensity (in green shading) and C_f (through line plots) for (a) optimal and (b) postoptimal SqW forcing, for which the two forcing phases and intraphase recovery clearly establish. Panel (c) shows postoptimum SinW forcing conceptualized based on past results of Agostini *et al.* [25,26], highlighting the more gradual and coupled phasewise variation of turbulence attenuation and recovery compared to SqW forcing.

reflects a minor recovery over its half-phase until the successive imposition of SSR, after which a more or less established attenuated turbulence response emerges. It is important to highlight that a distinct response of the TBL to the individual SSR phases emerges only when the half-phase extends significantly beyond $\lambda_x^+/2 \gg 500$, i.e., postoptimal conditions. For this case represented in Fig. 14(b), as subphase II is extended, a significant intraphase recovery of the near-wall turbulence becomes apparent.

For the postoptimal case, we observed the skin friction to reflect an out-of-phase response with respect to the turbulence attenuation. In association with subphase I, first a significant increase in C_f could be observed, followed by its continual decline over the rest of the half-phase. Although counterintuitive at first, this type of behavior could plausibly be explained by the different length scales over which we found C_f and turbulence to respond. The intraphase recovery was found to respond to a relatively short and viscous scale, which becomes particularly clear in the abrupt attenuation of $-\overline{uv}^+$ during subphase I and its subsequent recovery. On the other hand, our

experimental observations suggest skin friction responds to the forcing imposed low-energy state on a streamwise length scale of order δ_0. Moreover, the local increase in C_f during subphase I may be linked to the vortex-tilting mechanics [25,34] of the (partially) recovered turbulent streaks on the preceding half-phase. As a result of these dynamics, subphase I induces a substantial attenuation of turbulence, accompanied by a significant jump in C_f; subsequently, over subphase II, the skin friction is reduced in response to the imposed low energy state, while at the same time, the near-wall turbulence is already permitted to recover.

To discuss the impact of the forcing waveform, we compare the SqW and SinW at postoptimal forcing conditions in Figs. 14(b) and 14(c), where the latter is conceptualized based on the results of Agostini *et al.* [25]. Qualitatively, our results on skin friction and turbulence attenuation corroborate their findings. Interestingly, they noted an asymmetry between their drag-reduction phase and drag-increase phase, reminiscent of our subphase II and subphase I, respectively. As a consequence of the SinW forcing, however, these phases are not as distinct as the SqW but transition gradually from one to another, with both their regions of influence being proportional to λ_x. Accordingly, for the SinW, the SSR magnitude is inversely proportional to λ_x^+, thereby effectively lowering the forcing strength with increasing wavelength/period. Attesting to this, Ding *et al.* [38] have shown that the DR% in temporal SinW forcing scales well with the acceleration, defined as $a^+ = A^+/T^+$. On the other hand, the impulsive SSR response of SqW forcing enhances the asymmetry between the quasi-fixed subphase I and λ_x-dependent subphase II, so that the region of drag increase and turbulence attenuation is relatively short while the domain of C_f reduction and recovering turbulence is extended.

V. CONCLUDING REMARKS

We have presented an experimental study of wall-based transverse spanwise forcing by imposing a steady square wave (SqW), with the objective of reducing the wall-shear stress in a turbulent boundary layer (TBL). A dedicated spatial forcing setup, with a streamwise extent covering $\sim 11.5\delta_0$, has been implemented with the unique experimental ability to explore the TBL response to various independently controlled forcing parameters, viz., λ_x, A, and Re_τ. Specific to our experimental implementation is the square-wave forcing discretization, achieved with a series of spanwise running belts. Hence, one of the objectives is to distinguish how the SqW impacts the forcing compared to the sinusoidal waveform (SinW) generally considered in numerical studies. The present study focuses on the exploration of the streamwise evolution of a TBL at $\mathrm{Re}_\tau = 960$ subjected to increasing forcing wavelength, namely, $\lambda_x^+ = 471,\ 974,$ and 1884 at fixed $A^+ = 12$, in the streamwise fetch at the initiation as well as sufficiently downstream towards its fully established control state.

At the initiation of forcing, a strong control effect transient is established for all wavelengths considered, where a strongly reduced C_f state is attained within $x/\delta_0 \leqslant 1.5$. Qualitatively, the streamwise variation in C_f is consistent with the trends in the available literature for SinW forcing [13,23,59], suggesting that δ_0 is the relevant length scale given a universal collapse in the literature regardless of forcing type and actuation parameters. Similar trends are also associated with the attenuation of $\overline{uu}^+$ and $-\overline{uv}^+$, most notable among which is the strong initial attenuation of $-\overline{uv}^+$ by $\sim$75%–80% over a streamwise extent of only $0.1\delta_0$. When the wavelength increases beyond the generally recognized optimum of $\lambda_x^+ \approx 1000$ [10], to $\lambda_x^+ = 1884$, a significant recovery of turbulent stresses is observed within the forcing phase, with $-\overline{uv}^+$ reestablishing itself even towards its nonactuated stress levels. We confirm that the intraphase recovery is not dependent on the initial onset, as it is still significant for the postoptimum wavelength in the domain of fully established control (~ 9.5–$11.5\delta_0$). In this fully established domain, the flow modification is also characterized by the streamwise averaged turbulence statistics. These agree with the available literature on (sub-)optimum forcing. The postoptimum case shows a broadening of the $\overline{uu}^+$ peak, which we attribute to averaging across significantly varying phase-averaged statistics, exposed to either turbulence attenuation or recovery. Moreover, we established the control efficacy of the

actuator with regard to skin-friction drag reduction by means of a modified composite fit of the streamwise-time-averaged velocity profile. Qualitatively, our DR variation with λ_x^+ aligns with the previous findings of Viotti *et al.* [10] and Gatti and Quadrio [6], with a maximum of ∼38% for the near-optimum forcing case.

The particular turbulence modification behavior of the SqW strategy is associated with its Stokes strain rate (SSR) topology, which allows for the identification of two markedly different phases; subphase I associated with an impulsive imposition of high SSR, and subphase II of prolonged lingering Stokes strain (i.e., near-zero SSR). Based on the available literature, we hypothesized these regions to be linked to attenuation and recovery of the near-wall turbulence, respectively [25,26].

To better understand the intraphase recovery for SqW forcings relative to SinW, we explored the phasewise variation of the SSR through a modified Stokes layer model [21]. In the case of SinW forcing, the SSR varies slowly but continuously throughout the phase, reaching a maximum value where the wall velocity changes sign. In contrast, the SSR is imposed impulsively in the case of the SqW forcing (subphase I), with its instantaneous magnitude found to be about one order higher than for the SinW forcing at $\lambda_x^+ \approx 1000$, for the same forcing amplitude. This impulsively imposed SSR is concentrated at the x location where the switch in the spanwise wall-forcing direction occurs, followed by an extent of negligibly small SSR (subphase II) across the rest of the half-phase (owing to a constant spanwise wall velocity). For the SqW forcing, subphase I, where the forcing direction reverses, is largely independent of wavelength, while subphase II over the lingering half-phase extends in proportion to λ_x. In essence, the SqW enhances the asymmetry, proportional to λ_x, between the observed drag-reduction and drag-increasing subphases established for SinW forcing by Agostini *et al.* [25]. This link between the lingering subphase II with the intraphase recovery of turbulence only establishes itself for postoptimal conditions when the half-phase extends significantly beyond $\lambda_x^+/2 \gg 500$. The out-of-phase response between C_f and the near-wall turbulence may plausibly be explained by the different length scales on which the two phenomena respond, being δ_0 and a viscous length, respectively. Over the lingering subphase II, while the turbulence is already recovering, C_f declines/attenuates in response to the turbulence attenuation imposed by subphase I.

The experimental work and established SSR-related phenomenology provide valuable foundations for understanding flow-modifying mechanisms. These insights can facilitate future studies and inform new hypotheses, particularly regarding the postoptimal regime, wherefore several key open questions arise. First, as the SinW reduces in efficacy in proportion to λ_x [38], the question becomes as to how the intraphase recovery and C_f evolve over the lingering subphase II when extending to an even higher wavelength regime. An inquiry into the SqW and SinW performance at such conditions may become relevant in light of the outer-scaled actuation strategy proposed and tested by Marusic and co-workers [2,18,22]. A downside of the SqW-type forcing is the significant theoretical power requirements associated with the extended domain of a constant spanwise wall velocity. As such, the efficacy of the control strategy could be enhanced through waveform optimization by setting part of the wall velocity to $W_w = 0$ during the lingering subphase II. Therefore, investigating the TBL's response to the (partial) absence of forcing, as opposed to the lingering Stokes strain, is considered valuable. Moreover, the study's emphasis on SSR as a key driver of the drag-reduction mechanism may also offer valuable insights and support the development of future passive forcing implementations.

ACKNOWLEDGMENTS

We would like to extend our special gratitude to the teams at Dimple Aerospace B.V. and BerkelaarMRT B.V. for their invaluable assistance in the development of the experimental apparatus. We acknowledge and thank the technical staff of the wind tunnel laboratories at Delft University of Technology for their support. The financial support of The Netherlands Enterprise Agency, under Grant No. TSH21002, and the funding acquisition by Dimple Aerospace B.V. are gratefully

acknowledged by the authors. R.D. gratefully acknowledges financial support from the University of Melbourne's Postdoctoral Fellowship.

M.W.K.: conceptualization, methodology, investigation, formal analysis, writing—original draft. R.D.: conceptualization, investigation, writing—review and editing, supervision. F.F.J.S. and B.W.v.O.: writing—review and editing, supervision.

DATA AVAILABILITY

A full dataset accompanying the individual figures is available online and can be found at [60]; it contains the dimensional figure data as well as the relevant scaling parameter and atmospheric conditions. For completeness, we also provide the x-y contours of $\overline{U}$ and $\overline{vv}$ accompanying Figs. 7 and 11.

APPENDIX A: WALL-SHEAR STRESS DETERMINATION THROUGH THE MODIFIED COMPOSITE FIT

The well-established methodology of using a composite profile fit to the mean streamwise velocity profile, proposed by Chauhan *et al.* [44], is used here to obtain the mean friction velocity and the TBL thickness. Their original formulation is a combination of the inner-profile description by Musker [61] and an exponential formulation of the wake-profile based on high Re_τ measurements [62]. The composite profile considers log-law constants, $\kappa = 0.384$, $B = 4.17$ and is a function of the following variables: $U^+_{\mathrm{composite}}(U_\tau, \nu, \Pi, \delta)$, where Π is the wake parameter. Experimental studies are often subjected to an inherent uncertainty in the absolute wall-normal position of the first point from the wall [63]. This can be overcome by including a wall-normal offset (Δy) in the fitting parameters for the experimental data, as implemented previously by Rodríguez-López *et al.* [45]. They showed that the method performs accurately when the first datapoint is located $y^+ \leqslant 10$, to a 95% confidence interval for U_τ of $\pm 0.7\%$. Furthermore, they detail the method's robustness to near-wall distortion of the first point, for e.g., hot-wire conduction effects or biased near-wall PIV measurements. For the profiles that are considered in the work, spurious points, which were found up to a maximum of $y^+ < 4$, were manually removed before the final fitting procedure was performed.

The composite profile description is limited to canonical turbulent boundary layers. However, the formulations fall short if applied directly (i.e., without any modifications) to noncanonical cases, such as drag-reduced flows. To bridge this gap and quantify the DR%, we propose modifying the existing formulation by incorporating the additive constant (ΔB) to the log-law, during the data fitting procedure. This is based on the observation [6] that the mean streamwise velocity over an actuated surface, when scaled with the corresponding friction velocity, continues to exhibit inner scaling in the viscous sublayer while experiencing an upward shift (ΔB) in the logarithmic layer. We illustrate this in Fig. 15(a) by showing the modified composite profiles (compared to the canonical formulation) for DR% varying across 10:10:40, where $\overline{U}^*$ and y^* denote normalization by the corresponding friction velocity. Visually, one can observe the modification as an extension of the buffer region and the characteristic upward shift in $\overline{U}^*$. We show the quality of the fit to our experimental data in Fig. 15(b), depicting the reference case and actuated case from the discussion in Sec. III E. The fitting procedure is implemented in an iterative fashion using a sequential quadratic programming method. The objective is to minimize the mean quadratic error [Eq. (A1)] between the composite and experimental profiles. The experimental profiles are sampled on a logarithmic scale, where the vector pitch between the first points is retained, to give equal weighting to the inner and outer layers:

$$E = \overline{\sqrt{(\overline{U}^+_{\mathrm{composite}}(U_\tau, \Delta y, B, \nu, \Pi, \delta) - \overline{U}^+(U_\tau))^2}}. \tag{A1}$$

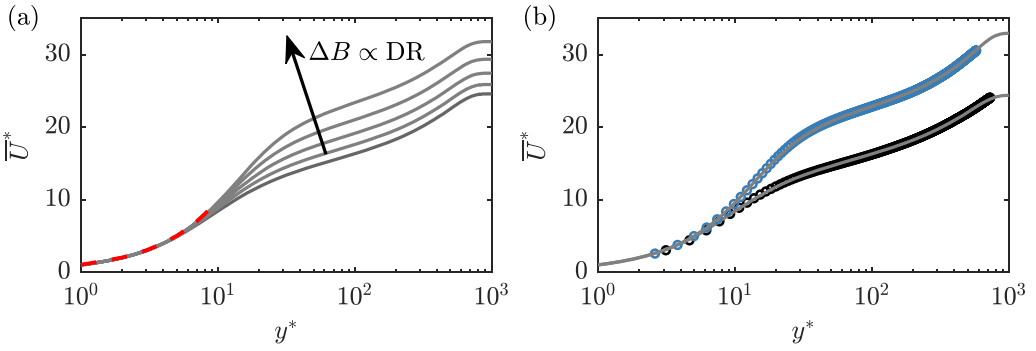

FIG. 15. (a) Variation of the modified composite profile with DR% ranging across 0:10:40. Red dashed lines denote $U^* = y^*$. (b) An example of the modified composite fit (gray shading) compared against the experimental data discussed in Sec. III E for the nonactuated (black) and actuated (blue) cases at $\lambda_x^+ = 942$, $A^+ = 12$.

The uncertainty in U_τ for the modified fit was assessed using FOV 2 data for the $\lambda_x^+ = 472$ case (Fig. 11). With $S = 2$, each datapoint represents the same half-phase location, expecting consistent U_τ values. After detrending to remove minor streamwise variations, Student's t distribution (i.e., eight samples) yielded a 95% confidence interval of $U_\tau \pm 0.75\%$, aligning with the classical formulation's uncertainty.

APPENDIX B: THE LAMINAR SOLUTION FOR MODIFIED SPATIAL STOKES LAYER

The analytical solution of the spatial Stokes layer (SSL) for SinW forcing, a derivative from the second Stokes problem (i.e., temporal transverse oscillations) [52], was initially presented by Viotti *et al.* [10]:

$$\widetilde{W}(x, y) = AC_x \mathrm{Re}\left[e^{\mathrm{i}k_x x}\mathrm{Ai}\left(-\frac{\mathrm{i}y}{\delta_x}e^{-\mathrm{i}4\pi/3}\right)\right], \tag{B1}$$

with $\delta_x = [\nu/(k_x u_{y,0})]^{1/3}$ as the penetration depth of the Stokes layer. In this relation, Re represents the real-valued component, i denotes the imaginary unit, Ai is the Airy function of the first kind, $C_x = \mathrm{Ai}(0)^{-1}$ is a normalization constant, and $u_{y,0}$ is the slope of the streamwise velocity profile at the wall. The Stokes layer solution has been validated extensively against both experimental and numerical data [10,22,64]. Given that we are imposing a different wall-boundary condition, specifically the square wave (SqW), the original solution for the SSL is no longer applicable. To address this, Knoop *et al.* [21] introduced a modified SSL that uses a Fourier series to prescribe the desired periodic boundary condition. Due to the linearity of the governing z-momentum equation, the elementary SSL solutions can be summed. This approach is inspired by Cimarelli *et al.* [57], who applied a similar technique for temporal forcing. Following this formulation, the wall velocity is given as

$$W_w(x) = A\sum_{n=-\infty}^{+\infty} B_n e^{\mathrm{i}k_x n x}, \tag{B2}$$

where n denotes the nth Fourier mode with complex coefficient B_n. We now superpose these solutions to obtain the modified SSL model for an arbitrary waveform:

$$\widetilde{W}(x, y) = AC_x \sum_{n=-\infty}^{+\infty} \mathrm{Re}\left[B_n e^{ik_x n x}\mathrm{Ai}\left(-\frac{iy}{\delta_x n^{-1/3}}e^{-i4\pi/3}\right)\right]. \tag{B3}$$

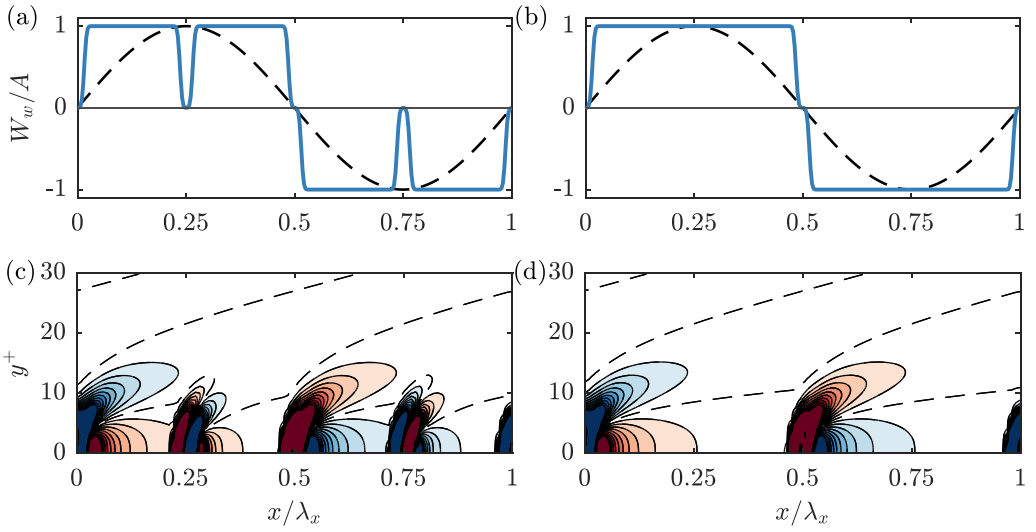

FIG. 16. A comparison of the modified SSL between (a), (c) the actual imposition of W_w, including 2-mm static region, and (b), (d) the simplified waveform. (a), (b) Imposed spanwise wall velocity for the case $\lambda_x^+ = 943$, with $S = 4$ belts, and (c), (d) their respective SSR response.

Consistent with classical formulations, Knoop *et al.* [21] demonstrated a good match between the modified SSL and experimental data. In its practical implementation, the SqW is convolved with a Gaussian function to prevent Gibbs phenomena, following a methodology similar to that used by Gallorini and Quadrio [20] for discrete STWs. A filter width of 1 mm was chosen carefully to minimize dispersive error while maintaining adequate spatial resolution.

For our discussion in Sec. III B, the waveform for the cases with $S > 2$ was simplified by removing the static 2 mm transition regions between belts that move with the same sign of W_w. Figure 16 compares the two scenarios, where Figs. 16(a) and 16(b) highlight differences in wall-based spanwise velocity, the inclusion of the static transition can be appreciated on the left [Figs. 16(a) and 16(c)]. We compare the SSR, the primary quantity associated with the control effect in Figs. 16(c) and 16(d), revealing an additional imposition of a respective positive and negative (and vice versa) SSR in Fig. 16(c). Our results (e.g., Fig. 7) do not evidence a substantial impact of these static regions on the response of the TBL, with modifications only observed corresponding to a change in the W_w sign. It is with this justification that we chose to simplify the wall velocity to better illustrate the discussion on the SSR.

[1] P. Ricco, M. Skote, and M. A. Leschziner, A review of turbulent skin-friction drag reduction by near-wall transverse forcing, Prog. Aerosp. Sci. **123**, 100713 (2021).

[2] I. Marusic, D. Chandran, A. Rouhi, M. K. Fu, D. Wine, B. Holloway, D. Chung, and A. J. Smits, An energy-efficient pathway to turbulent drag reduction, Nat. Commun. **12**, 5805 (2021).

[3] S. Ghebali, S. I. Chernyshenko, and M. A. Leschziner, Can large-scale oblique undulations on a solid wall reduce the turbulent drag? Phys. Fluids **29**, 105102 (2017).

[4] M. van Nesselrooij, L. Veldhuis, B. Van Oudheusden, and F. Schrijer, Drag reduction by means of dimpled surfaces in turbulent boundary layers, Exp. Fluids **57**, 142 (2016).

[5] M. Quadrio, P. Ricco, and C. Viotti, Streamwise-travelling waves of spanwise wall velocity for turbulent drag reduction, J. Fluid Mech. **627**, 161 (2009).

[6] D. Gatti and M. Quadrio, Reynolds-number dependence of turbulent skin-friction drag reduction induced by spanwise forcing, J. Fluid Mech. **802**, 553 (2016).
[7] J. Kim and F. Hussain, Propagation velocity of perturbations in turbulent channel flow, Phys. Fluids A: Fluid Dyn. **5**, 695 (1993).
[8] W. J. Jung, N. Mangiavacchi, and R. Akhavan, Suppression of turbulence in wall–bounded flows by high–frequency spanwise oscillations, Phys. Fluids **4**, 1605 (1992).
[9] F. Laadhari, L. Skandaji, and R. Morel, Turbulence reduction in a boundary layer by a local spanwise oscillating surface, Phys. Fluids **6**, 3218 (1994).
[10] C. Viotti, M. Quadrio, and P. Luchini, Streamwise oscillation of spanwise velocity at the wall of a channel for turbulent drag reduction, Phys. Fluids **21**, 115109 (2009).
[11] A. Yakeno, Y. Hasegawa, and N. Kasagi, Spatio-temporally periodic control for turbulent friction drag reduction, in *Proceedings of the 6th International Symposium on Turbulence and Shear Flow Phenomena* (Begell House, Danbury, Connecticut, 2009), pp. 598–603.
[12] M. Skote, Turbulent boundary layer flow subject to streamwise oscillation of spanwise wall-velocity, Phys. Fluids **23**, 081703 (2011).
[13] M. Skote, Comparison between spatial and temporal wall oscillations in turbulent boundary layer flows, J. Fluid Mech. **730**, 273 (2013).
[14] E. Hurst, Q. Yang, and Y. M. Chung, The effect of Reynolds number on turbulent drag reduction by streamwise travelling waves, J. Fluid Mech. **759**, 28 (2014).
[15] M. Mishra and M. Skote, Drag reduction in turbulent boundary layers with half wave wall oscillations, Math. Probl. Eng. **2015**, 253249 (2015).
[16] F. Auteri, A. Baron, M. Belan, G. Campanardi, and M. Quadrio, Experimental assessment of drag reduction by traveling waves in a turbulent pipe flow, Phys. Fluids **22**, 115103 (2010).
[17] J. Bird, M. Santer, and J. F. Morrison, Experimental control of turbulent boundary layers with in-plane travelling waves, Flow Turbul. Combust. **100**, 1015 (2018).
[18] D. Chandran, A. Zampiron, A. Rouhi, M. K. Fu, D. Wine, B. Holloway, A. J. Smits, and I. Marusic, Turbulent drag reduction by spanwise wall forcing. Part 2. High-Reynolds-number experiments, J. Fluid Mech. **968**, A7 (2023).
[19] R. O. Kiesow and M. W. Plesniak, Near-wall physics of a shear-driven three-dimensional turbulent boundary layer with varying crossflow, J. Fluid Mech. **484**, 1 (2003).
[20] E. Gallorini and M. Quadrio, Spatial discretization effects in spanwise forcing for turbulent drag reduction, J. Fluid Mech. **982**, A11 (2024).
[21] M. W. Knoop, F. H. Hartog, F. F. J. Schrijer, O. W. G. van Campenhout, M. van Nesselrooij, and B. W. van Oudheusden, Experimental assessment of square-wave spatial spanwise forcing of a turbulent boundary layer, Exp. Fluids **65**, 65 (2024).
[22] R. Deshpande, A. Zampiron, D. Chandran, A. J. Smits, and I. Marusic, Near-wall flow statistics in high-Re_τ drag-reduced turbulent boundary layers, Flow Turbul. Combust. **113**, 3 (2024).
[23] P. Ricco and S. Wu, On the effects of lateral wall oscillations on a turbulent boundary layer, Exp. Therm. Fluid Sci. **29**, 41 (2004).
[24] E. Touber and M. A. Leschziner, Near-wall streak modification by spanwise oscillatory wall motion and drag-reduction mechanisms, J. Fluid Mech. **693**, 150 (2012).
[25] L. Agostini, E. Touber, and M. Leschziner, The turbulence vorticity as a window to the physics of friction-drag reduction by oscillatory wall motion, Int. J. Heat Fluid Flow **51**, 3 (2015).
[26] L. Agostini, E. Touber, and M. A. Leschziner, Spanwise oscillatory wall motion in channel flow: Drag-reduction mechanisms inferred from DNS-predicted phase-wise property variations at $\mathrm{Re}_\tau = 1000$, J. Fluid Mech. **743**, 606 (2014).
[27] A. Rouhi, M. K. Fu, D. Chandran, A. Zampiron, A. J. Smits, and I. Marusic, Turbulent drag reduction by spanwise wall forcing. Part 1. Large-eddy simulations, J. Fluid Mech. **968**, A6 (2023).
[28] R. Akhavan, W. Jung, and N. Mangiavacchi, Control of wall turbulence by high frequency spanwise oscillations, in *3rd Shear Flow Conference* (American Institute of Aeronautics and Astronautics, Reston, Virginia, 1993), pp. 93–3282.

[29] A. Baron and M. Quadrio, Turbulent drag reduction by spanwise wall oscillations, Appl. Sci. Res. **55**, 311 (1996).
[30] J. Jiménez and A. Pinelli, The autonomous cycle of near-wall turbulence, J. Fluid Mech. **389**, 335 (1999).
[31] P. Ricco, Modification of near-wall turbulence due to spanwise wall oscillations, J. Turbul. **5**, 024 (2004).
[32] K. U. Kempaiah, F. Scarano, G. E. Elsinga, B. W. Van Oudheusden, and L. Bermel, 3-dimensional particle image velocimetry based evaluation of turbulent skin-friction reduction by spanwise wall oscillation, Phys. Fluids **32**, 085111 (2020).
[33] K.-S. Choi and B. R. Clayton, The mechanism of turbulent drag reduction with wall oscillation, Int. J. Heat Fluid Flow **22**, 1 (2001).
[34] M. Umair and S. Tardu, Vorticity transport in a turbulent channel flow subjected to streamwise travelling waves, J. Fluid Mech. **967**, A9 (2023).
[35] Y. Miyake, K. Tsujimoto, and M. Takahashi, On the mechanism of drag reduction of near-wall turbulence by wall oscillation, JSME Int. J. Ser. B **40**, 558 (1997).
[36] P. Orlandi and J. Jiménez, On the generation of turbulent wall friction, Phys. Fluids **6**, 634 (1994).
[37] P. Bradshaw and N. Pontikos, Measurements in the turbulent boundary layer on an 'infinite' swept wing, J. Fluid Mech. **159**, 105 (1985).
[38] L. Ding, L. F. Sabidussi, B. C. Holloway, M. Hultmark, and A. J. Smits, Acceleration is the key to drag reduction in turbulent flow, Proc. Natl. Acad. Sci. USA **121**, e2403968121 (2024).
[39] M. P. Schultz and K. A. Flack, The rough-wall turbulent boundary layer from the hydraulically smooth to the fully rough regime, J. Fluid Mech. **580**, 381 (2007).
[40] G. Dacome, R. Mörsch, M. Kotsonis, and W. J. Baars, Opposition flow control for reducing skin-friction drag of a turbulent boundary layer, Phys. Rev. Fluids **9**, 064602 (2024).
[41] See Supplemental Material at http://link.aps.org/supplemental/10.1103/PhysRevFluids.10.064607 for a video recording of the spatial wall forcing apparatus.
[42] J. Jiménez, Turbulent flows over rough walls, Annu. Rev. Fluid Mech. **36**, 173 (2004).
[43] J. Westerweel and F. Scarano, Universal outlier detection for PIV data, Exp. Fluids **39**, 1096 (2005).
[44] K. A. Chauhan, P. A. Monkewitz, and H. M. Nagib, Criteria for assessing experiments in zero pressure gradient boundary layers, Fluid Dyn. Res. **41**, 021404 (2009).
[45] E. Rodríguez-López, P. J. Bruce, and O. R. Buxton, A robust post-processing method to determine skin friction in turbulent boundary layers from the velocity profile, Exp. Fluids **56**, 68 (2015).
[46] P. Schlatter and R. Örlü, Assessment of direct numerical simulation data of turbulent boundary layers, J. Fluid Mech. **659**, 116 (2010).
[47] J. Lee, Kevin, J. Monty, and N. Hutchins, Validating under-resolved turbulence intensities for PIV experiments in canonical wall-bounded turbulence, Exp. Fluids **57**, 129 (2016).
[48] B. M. Wilson and B. L. Smith, Uncertainty on PIV mean and fluctuating velocity due to bias and random errors, Meas. Sci. Technol. **24**, 035302 (2013).
[49] J. Kim, Physics and control of wall turbulence for drag reduction, Philos. Trans. R. Soc. A **369**, 1396 (2011).
[50] J. A. Sillero, J. Jiménez, and R. D. Moser, Two-point statistics for turbulent boundary layers and channels at Reynolds numbers up to $\delta^+ \approx 2000$, Phys. Fluids **26**, 105109 (2014).
[51] M. Skote, M. Mishra, and Y. Wu, Wall oscillation induced drag reduction zone in a turbulent boundary layer, Flow Turbul. Combust. **102**, 641 (2019).
[52] G. Stokes, On the effect of the internal friction of fluids on the motion of pendulums, Trans. Cambridge Philos. Soc. **9**, 8 (1851).
[53] M. Quadrio and P. Ricco, Critical assessment of turbulent drag reduction through spanwise wall oscillations, J. Fluid Mech. **521**, 251 (2004).
[54] K. Fukagata, K. Iwamoto, and N. Kasagi, Contribution of Reynolds stress distribution to the skin friction in wall-bounded flows, Phys. Fluids **14**, L73 (2002).
[55] A. Elnahhas and P. L. Johnson, On the enhancement of boundary layer skin friction by turbulence: An angular momentum approach, J. Fluid Mech. **940**, A36 (2022).

[56] O. Blesbois, S. I. Chernyshenko, E. Touber, and M. A. Leschziner, Pattern prediction by linear analysis of turbulent flow with drag reduction by wall oscillation, J. Fluid Mech. **724**, 607 (2013).
[57] A. Cimarelli, B. Frohnapfel, Y. Hasegawa, E. De Angelis, and M. Quadrio, Prediction of turbulence control for arbitrary periodic spanwise wall movement, Phys. Fluids **25**, 075102 (2013).
[58] S. J. Kline, W. C. Reynolds, F. A. Schraub, and P. W. Runstadler, The structure of turbulent boundary layers, J. Fluid Mech. **30**, 741 (1967).
[59] S. Lardeau and M. A. Leschziner, The streamwise drag-reduction response of a boundary layer subjected to a sudden imposition of transverse oscillatory wall motion, Phys. Fluids **25**, 075109 (2013).
[60] An accompanying dataset is made available in the 4TU ResearchData repository at doi: 10.4121/adb0b003-4912-4bdb-b12f-e56d18c3b937.
[61] A. J. Musker, Explicit expression for the smooth wall velocity distribution in a turbulent boundary layer, AIAA J. **17**, 655 (1979).
[62] H. M. Nagib, C. Christophorou, and P. A. Monkewitz, High Reynolds number turbulent boundary layers subjected to various pressure-gradient conditions, in *Proceedings of the IUTAM Symposium 2004, Göttingen, Germany* (Springer, Dordrecht, 2006), pp. 383–394.
[63] R. Örlü, J. H. Fransson, and P. H. Alfredsson, On near wall measurements of wall bounded flows—The necessity of an accurate determination of the wall position, Prog. Aerosp. Sci. **46**, 353 (2010).
[64] K.-S. Choi, Near-wall structure of turbulent boundary layer with spanwise-wall oscillation, Phys. Fluids **14**, 2530 (2002).